

## OPEN ACCESS

# A detailed de Haas–van Alphen effect study of the overdoped cuprate $\text{Ti}_2\text{Ba}_2\text{CuO}_{6+\delta}$

To cite this article: P M C Rourke *et al* 2010 *New J. Phys.* **12** 105009

View the [article online](#) for updates and enhancements.

## You may also like

- [Two gaps make a high-temperature superconductor?](#)  
S Hüfner, M A Hossain, A Damascelli et al.
- [Electronic inhomogeneity in Pb-substituted  \$\text{Bi}\_2\text{Sr}\_2\text{CuO}\_{6+x}\$  studied by STM/STS measurements](#)  
K Kudo, T Nishizaki, N Okumura et al.
- [Growth and post-annealing studies of  \$\text{Bi}\_2\text{Sr}\_{1-x}\text{La}\_x\text{CuO}\_{6+x}\$  \(0x1.00\) single crystals](#)  
Huiqian Luo, Peng Cheng, Lei Fang et al.

## A detailed de Haas–van Alphen effect study of the overdoped cuprate $\text{Ti}_2\text{Ba}_2\text{CuO}_{6+\delta}$

P M C Rourke<sup>1</sup>, A F Bangura<sup>1</sup>, T M Benseman<sup>2</sup>, M Matusiak<sup>2</sup>,  
J R Cooper<sup>2</sup>, A Carrington<sup>1</sup> and N E Hussey<sup>1,3</sup>

<sup>1</sup> H H Wills Physics Laboratory, University of Bristol, Tyndall Avenue,  
Bristol BS8 1TL, UK

<sup>2</sup> Physics Department, Cavendish Laboratory, University of Cambridge,  
J J Thomson Avenue, Cambridge CB3 0HE, UK

E-mail: [n.e.hussey@bristol.ac.uk](mailto:n.e.hussey@bristol.ac.uk)

*New Journal of Physics* **12** (2010) 105009 (29pp)

Received 23 July 2010

Published 29 October 2010

Online at <http://www.njp.org/>

doi:10.1088/1367-2630/12/10/105009

**Abstract.** We report a detailed quantum oscillation study of the overdoped cuprate  $\text{Ti}_2\text{Ba}_2\text{CuO}_{6+\delta}$  at two different doping levels ( $T_c = 10$  and 26 K). The derived Fermi surface size and topology complement earlier angle-dependent magnetoresistance studies and confirm the existence of a large quasi-cylindrical hole-doped Fermi surface with a small, but finite,  $c$ -axis warping. An accurate determination of the hole concentration reveals that superconductivity in  $\text{Ti}_2\text{Ba}_2\text{CuO}_{6+\delta}$  does not follow the universal  $T_c(p)$  parabola for cuprate families and survives up to a larger doping of  $p_c = 0.31$ . The observation of quantum oscillations for both dopings demonstrates that Fermi liquid behaviour is not confined to the edge of the superconducting dome, but is robust up to at least  $0.3T_c^{\text{max}}$ . Moreover, the observation of such well-resolved oscillations implies that the physical properties of overdoped  $\text{Ti}_2\text{Ba}_2\text{CuO}_{6+\delta}$  are determined by a single, spatially homogeneous electronic ground state. Finally, analysis of the different quasiparticle masses points towards a purely magnetic or electronic pairing mechanism.

<sup>3</sup> Author to whom any correspondence should be addressed.

**Contents**

<b>1. Introduction</b>	<b>2</b>
<b>2. Quantum oscillations and damping factors</b>	<b>4</b>
<b>3. Fermi surface warping</b>	<b>7</b>
<b>4. Experimental details</b>	<b>10</b>
<b>5. Results</b>	<b>10</b>
<b>6. Band structure</b>	<b>20</b>
<b>7. Discussion</b>	<b>23</b>
<b>8. Conclusion</b>	<b>26</b>
<b>Acknowledgments</b>	<b>27</b>
<b>References</b>	<b>27</b>

**1. Introduction**

Understanding the high-temperature superconducting cuprates is, without doubt, one of the most formidable challenges in condensed matter physics [1]. In addition to their high transition temperatures, their anomalous normal state transport properties (above  $T_c$ ) [2] are often cited as the most striking example to date of the breakdown of Landau's Fermi liquid description of metals. One of the fundamental signatures of a Fermi liquid is of course the Fermi surface, the locus in reciprocal space of long-lived quasiparticle excitations that govern the electronic properties at low temperatures. In conventional metals, these excitations have well-defined momenta with components in all three dimensions. The failure to unambiguously observe such an entity in cuprates in the two decades following their discovery, coupled with their unusual, highly two-dimensional (2D) electronic properties, led to an intensive theoretical search for novel (strongly correlated) electronic ground states in two dimensions [3], a search that continues to this day.

During the course of the first 20 years of cuprate research, various physical properties, particularly in the overdoped cuprates, were found to be consistent with conventional Fermi-liquid behaviour, but none of the experimental results could truly be considered as direct proof of the existence of fermionic quasiparticles around a closed and fully coherent Fermi surface. The electronic specific heat of  $\text{YBa}_2\text{Cu}_3\text{O}_{6+\delta}$  (Y123), for example, was found to be composed of fermionic excitations, albeit with a low Fermi energy and a pseudogap [4], the Wiedemann–Franz law was found to be obeyed in overdoped  $\text{Tl}_2\text{Ba}_2\text{CuO}_{6+\delta}$  (Tl2201) [5], and in heavily overdoped non-superconducting  $\text{La}_{2-x}\text{Sr}_x\text{CuO}_4$  (LSCO), the in-plane resistivity followed a strictly quadratic temperature dependence at low  $T$  [6]. In overdoped  $\text{Bi}_2\text{Sr}_2\text{CaCu}_2\text{O}_{8+\delta}$  (Bi2212), quasiparticle-like peaks were detected in the energy–density curves derived from angle-resolved photo-emission spectroscopy (APRES) experiments at all Fermi wavevectors in the normal state [7], although their widths near the zone boundaries were often too broad (up to 0.1 eV) to be considered as conclusive evidence for the long-lived quasiparticle states predicted by density functional theory band-structure calculations. Finally, evidence for a large three-dimensional (3D) Fermi surface emerged in 2003 through the analysis of angle-dependent magnetoresistance (ADMR) data for Tl2201 [8]. Being a semi-classical

phenomenon, however, the observation of ADMR alone could not provide any definitive conclusions about the quantum mechanical nature of the underlying electronic ground state.

Arguably the most concrete signature of fermionic excitations in a metal is the observation of quantum oscillations. In the early days of high- $T_c$  cuprate research, low-frequency oscillations of the (inverse) magnetization, the de Haas–van Alphen (dHvA) effect, were reported in optimally doped Y123 and overdoped Tl2201 [9, 10]. However, the signal-to-noise level in these measurements was very low and it was demonstrated that the claimed peaks in the frequency spectrum could easily be explained as artefacts of the data analysis [11]. Importantly, as sample quality and maximum field improved, there were no further reports of oscillations and so it was concluded by many that these early experiments did not, in fact, observe quantum oscillations. This failure to observe genuine quantum oscillations tended to suggest that fermionic quasiparticles were absent in these strongly correlated metals; the combined effects of low dimensionality and the proximity to a Mott insulating phase were confining and intensifying the electron correlations to such an extent that a Fermi surface of well-defined quasiparticle excitations did not survive.

In the spring of 2007, an important advancement was made by the observation of quantum oscillations in the Hall and longitudinal magnetoresistance of underdoped Y123 [12], a breakthrough that was followed quickly by similar reports of oscillations in underdoped YBa<sub>2</sub>Cu<sub>4</sub>O<sub>8</sub> (Y124) [13, 14], and later in overdoped Tl2201 [15, 16] and the electron-doped compound Nd<sub>2-x</sub>Ce<sub>x</sub>CuO<sub>4</sub> (NCCO) [17]. While the origin and nature of the pockets responsible for the oscillations in the Y-based cuprates remain the subject of intense debate, quantum oscillations observed in single-layer, single-band Tl2201 appeared to provide clear and unambiguous evidence that the charge carriers, at least in the overdoped, superconducting CuO<sub>2</sub> planes, are indeed fermionic quasiparticles.

In this paper, we report a detailed analysis of angle-dependent dHvA data for overdoped Tl2201 with two different  $T_c$  values from which important information pertaining to the bulk electronic structure and the superconductivity of the doped CuO<sub>2</sub> planes is obtained. Our results show that a generalized Fermi-liquid picture extends into the high- $T_c$  phase of overdoped cuprates and is not confined to the edge of the superconducting dome. We also show that overdoped Tl2201 has a highly homogeneous electronic state on the scale of the cyclotron radius ( $r_c \gtrsim 1200$  Å at 40 T). Our precise determination of the Fermi surface volume reveals that superconductivity in Tl2201 survives up to a hole doping of  $p_c = 0.31$ , significantly beyond that inferred for LSCO and by extension other cuprate families [18]. Finally, the dHvA mass is found to be relatively insensitive to the hole concentration  $1 + p$  and seems to result from an overall band-narrowing rather than strong renormalization near the Fermi level. These two latter facts seem to rule out pairing mechanisms involving low-frequency bosons; however, as we will describe later, a strong  $k$  dependence of the quasiparticle renormalization cannot be ruled out.

In section 2, we provide a brief description of quantum oscillations and the various damping factors from which important details of the nature of the quasiparticles can be gleaned. Section 3 focuses on the key issue of dimensionality in a quasi-2D metal, with specific reference to the  $c$ -axis warping expected in body-centred tetragonal Tl2201. Sections 4 and 5 contain experimental details and results, respectively. In section 6, we compare our results to *ab-initio* band-structure calculations, and in section 7, we discuss the implications of these findings for our understanding of the cuprate phase diagram. Our conclusions are summarized in section 8.

## 2. Quantum oscillations and damping factors

The observation of the phenomenon of quantum oscillations has been used for more than 50 years [19] as one of the most direct and precise means of experimentally measuring the Fermi surface topology of a crystalline conductor. When a metal is subjected to a magnetic field  $\mathbf{B} = (B, \varphi, \theta)$ , the allowed quasiparticle states lie on quantized Landau tubes—concentric cylinders aligned along the direction of the field whose  $\mathbf{k}$ -space radii increase with increasing  $B$ . Only the portions of each tube lying below the chemical potential, and therefore inside the Fermi surface, contain occupied states. As the field strength  $B$  is increased, the tubes get larger (in  $\mathbf{k}$  space) and leave the Fermi surface one by one, depopulating as they do so. This repeated depopulation results in oscillations of the free energy that are periodic in  $1/B$ , with the frequencies

$$F = \frac{\hbar}{2\pi e} \mathcal{A}_{\text{ext}} \quad (1)$$

corresponding to extrema  $\mathcal{A}_{\text{ext}}$  in the cross-sectional areas of the Fermi surface perpendicular to  $\mathbf{B}$ . Such quantum oscillations show up in many measurable physical quantities; the dHvA effect employed in the present study refers to oscillations manifested in the bulk magnetization or torque [19]:

$$\tilde{\tau} = A \sin \left[ 2\pi \left( \frac{F}{B} \right) + \xi \right]. \quad (2)$$

In addition to the oscillation frequency  $F$ , a great deal of information can be obtained by paying attention to the dependence of the oscillation amplitude  $A$  on the temperature and the strength and orientation of the magnetic field. For a quasi-2D system such as Tl2201, where the Fermi surface is roughly cylindrical, the oscillation frequency follows the form

$$F(\theta) \approx F_0 / \cos \theta, \quad (3)$$

where  $\theta$  is the polar magnetic field angle measured relative to the crystalline  $c$ -axis, and  $F_0$  is the oscillation frequency obtained when the magnetic field is applied parallel to the  $c$ -axis. The overall field- and temperature-dependent oscillation amplitude is given by

$$A(\mathbf{B}, T) = A_0 \prod_i R_i(\mathbf{B}, T), \quad (4)$$

wherein  $A_0$  contains all field- and temperature-independent amplitude information. The set of multiplicative  $R_i$  terms represents modifications to the oscillation strength from various physical sources, discussed in more detail below. Many of the  $R_i$  terms arise from processes that dephase and therefore damp out the quantum oscillations. The terms that are of importance to our experiment are those due to the torque measurement technique ( $R_{\text{torque}}$ ), blurring of the Fermi surface at finite temperatures ( $R_T$ ), scattering-induced broadening of the Landau levels ( $R_D$ ), crystalline mosaicity ( $R_{\text{mos}}$ ), doping inhomogeneity ( $R_{\text{dop}}$ ), spin-splitting of the Fermi surface ( $R_s$ ) and Fermi surface  $c$ -axis warping ( $R_{\text{warp}}$ ; see section 3), such that equation (4) becomes

$$A(B, \varphi, \theta, T) = A_0 R_{\text{torque}} R_T R_D R_{\text{mos}} R_{\text{dop}} R_s R_{\text{warp}}. \quad (5)$$

In Tl2201,  $\varphi$  refers to the azimuthal magnetic field angle measured relative to the copper–oxygen bond direction.

As explained in section 4, in our experiments we measure the torque  $\tau$  applied to the sample by the magnetic field as it is held semi-rigidly on a microcantilever. For a quasi-2D metal, in which additionally  $F_0 \gg B$ , this leads to a modification of the oscillation amplitude (compared to the oscillatory magnetization along the  $c$ -axis  $\tilde{M}_{\parallel c}$ ) of [19]–[21]

$$R_{\text{torque}}(B, \theta) = B |\sin \theta|. \quad (6)$$

The primary challenge that must be overcome in order to observe quantum oscillations lies in the fact that, in practice, the oscillatory signals are often strongly damped by dephasing processes. Such processes cause a single well-defined quantum oscillation to be replaced by a superposition of oscillations in which the frequency (or equivalently the phase) varies slightly. The destructive interference arising from this phase smearing effect reduces the amplitude of the measured oscillatory signal by a factor  $R_z$  given by the Fourier transform of the phase smearing distribution function  $D(z)$  [19]:

$$R_z(\lambda) = \int_{-\infty}^{\infty} e^{i\lambda z} D(z) dz \Big/ \int_{-\infty}^{\infty} D(z) dz. \quad (7)$$

The Fourier transform is taken with respect to the variable  $\lambda$ , which quantifies how much the oscillation phase is changed by a small change in the physical parameter of interest (here labelled  $z$ ):

$$\lambda = \frac{2\pi}{B} \frac{\partial F}{\partial z}. \quad (8)$$

One example of a dephasing effect occurs when a finite temperature  $T$  causes states within  $k_B T$  of the Fermi level to be occupied. This can be thought of as superimposing a continuum of extremal area frequencies distributed over this energy interval. In standard Lifshitz–Kosevich (LK) theory, the relevant phase smearing distribution function is the negative derivative with respect to energy of the Fermi function, leading to a damping term [19]

$$R_T(B, \theta, T) = \left[ \frac{2\pi^2 k_B m_{\text{therm}}^* T}{e\hbar B \cos \theta} \right] \Big/ \sinh \left[ \frac{2\pi^2 k_B m_{\text{therm}}^* T}{e\hbar B \cos \theta} \right], \quad (9)$$

in which  $k_B$  is the Boltzmann constant and  $m_{\text{therm}}^*$  is the thermodynamic quasiparticle effective mass—the same effective mass as that measured by specific heat experiments.  $m_{\text{therm}}^*$  is renormalized relative to the band mass  $m_b$  by electron–phonon interactions and the spin-symmetric part of the electron–electron interactions, but not by the spin-antisymmetric (Stoner) part of the electron–electron interactions [21, 22]. Since  $R_T$  is the only temperature-dependent damping factor, it may be used to determine  $m_{\text{therm}}^*$  from the measured temperature dependence of the quantum oscillation amplitude. Note that the standard LK form of  $R_T$  shown in equation (9) does not include contributions from marginal Fermi liquid effects [23], although such deviations are typically only apparent at the lowest temperatures [24, 25].

Small- and large-angle quasiparticle scattering from crystal impurities dephases quantum oscillations by broadening the Landau energy levels (blurring the Landau tubes). This broadening can be represented by a Lorentzian phase smearing distribution function, whose Fourier transform leads to the exponential form of the so-called Dingle impurity damping term. For a quasi-2D compound with an isotropic scattering mean free path  $\ell_0$ , the Dingle term can be written as [19]

$$R_D(B, \theta) = \exp \left\{ -\pi \sqrt{\frac{2\hbar F_0}{e}} \frac{1}{\ell_0 B \cos \theta} \right\}. \quad (10)$$

If the sample being measured is composed of a mosaic of smaller crystallites, with a small distribution of angles around the nominal crystal orientation, further dephasing will occur. Assuming the distribution of crystallite angles is a simple Gaussian function

$$D(z) \propto \exp(-z^2), \quad (11)$$

where  $z = \theta/\delta\theta$  with  $\delta\theta$  being the half-width of the Gaussian, equation (8) becomes

$$\lambda = \frac{2\pi}{B} \frac{\partial F}{\partial \theta} \delta\theta, \quad (12)$$

and equation (7) reduces to [19, 26]

$$\begin{aligned} R_{\text{mos}}(B, \theta) &= \exp\left\{-\frac{1}{4}\lambda^2\right\} \\ &= \exp\left\{-\left[\frac{\pi}{B} \left(\frac{\partial F}{\partial \theta}\right) \delta\theta\right]^2\right\} \\ &= \exp\left\{-\left[\frac{\pi F_0}{B} \left(\frac{\sin \theta}{\cos^2 \theta}\right) \delta\theta\right]^2\right\}. \end{aligned} \quad (13)$$

Similarly, dephasing will result if the hole doping (and therefore Fermi volume) varies across the sample. If, as above, the distribution of dopings is assumed to be Gaussian about the nominal hole doping  $p$  per in-plane Cu atom, the associated oscillation damping factor is

$$\begin{aligned} R_{\text{dop}}(B, \theta) &= \exp\left\{-\left[\frac{\pi}{B} \left(\frac{\partial F}{\partial p}\right) \delta p\right]^2\right\} \\ &= \exp\left\{-\left[\frac{\pi}{B \cos \theta} \left(\frac{\partial F_0}{\partial p}\right) \delta p\right]^2\right\} \\ &= \exp\left\{-\left[\frac{\pi^2 \hbar \delta p}{a^2 e B \cos \theta}\right]^2\right\}, \end{aligned} \quad (14)$$

where  $\delta p$  is the half-width of the Gaussian,  $a$  is the in-plane lattice parameter, and hole counting is used to obtain

$$\begin{aligned} F_0(p) &= \frac{\hbar}{2\pi e} \mathcal{A}_{\text{ext},0} \\ &= \frac{\hbar}{2\pi e} \left[ \frac{1+p}{2} \left( \frac{2\pi}{a} \right)^2 \right] \\ &= \frac{\pi \hbar}{a^2 e} (1+p). \end{aligned} \quad (15)$$

The final effect to be considered in this section is that due to spin-splitting of the Fermi surface by the applied magnetic field. Depending on the direction of the magnetic field, oscillations arising from the majority-spin and minority-spin Fermi surface sheets will interfere constructively or destructively, resulting in dramatic changes of the observed quantum



oscillation amplitude. For a quasi-2D system in which the magnetic field splits the Fermi surface without distorting it, the amplitude modification factor due to spin-splitting is

$$R_s(\theta) = \left| \cos\left(\frac{\pi g m_{\text{sus}}^*}{2m_e \cos \theta}\right) \right|, \quad (16)$$

where the spin  $g$ -factor is assumed to be equal to 2 for the purposes of our study,  $m_e$  is the bare electron mass, and  $m_{\text{sus}}^*$  is the susceptibility quasiparticle effective mass.  $m_{\text{sus}}^*$  is renormalized relative to the band mass  $m_b$  by both the spin-symmetric and spin-antisymmetric (Stoner) parts of the electron–electron interactions, but not by the electron–phonon interactions [21, 22]. Thus, for a given material,  $m_{\text{sus}}^*$  need not be the same as  $m_{\text{therm}}^*$ , and indeed can be either larger or smaller than  $m_{\text{therm}}^*$  (for example,  $m_{\text{sus}}^*/m_{\text{therm}}^* \sim 1.6$  for the  $\gamma$  sheet of  $\text{Sr}_2\text{RuO}_4$  [21] and  $\sim 0.6$  for the  $\sigma$  sheet of  $\text{MgB}_2$  [27]).

If the spin-splitting is linear in  $B$ , the difference in  $k$ -space extremal areas of the spin-up and spin-down Fermi surface sheets is also linear in  $B$  and hence the phase difference between the two oscillatory terms is constant as a function of the field. A situation known as a ‘spin zero’ occurs when, at a particular angle  $\theta_0$ , there is perfect destructive interference. Locating the spin zeros of a given compound allows  $m_{\text{sus}}^*$  to be determined, although the highly nonlinear nature of equation (16) means that this must be done with care. Specifically, the presence of a spin zero at angle  $\theta_0$  does not correspond to a unique value of  $m_{\text{sus}}^*$ , but rather to an infinite ‘magic list’ of compatible values

$$\frac{m_{\text{sus}}^*}{m_e} = \frac{j}{2} \cos \theta_0; \quad j = 1, 3, 5, 7, 9, \dots \quad (17)$$

In order to pin down  $m_{\text{sus}}^*$  to a particular value on the magic list, at least two spin zeros must be observed. Furthermore, an  $m_{\text{sus}}^*$  that is numerically similar to a value on the magic list but that is not on the list itself may correspond to an entirely different set of spin zeros. For example,  $\theta_0 = 27.6^\circ$  is associated with  $m_{\text{sus}}^* = \{0.44m_e, 1.33m_e, 2.22m_e, 3.10m_e, 3.99m_e, 4.87m_e, 5.76m_e, 6.65m_e, 7.53m_e, 8.42m_e, \dots\}$ ; figure 1 shows the angle dependence of  $R_s$  for several values of  $m_{\text{sus}}^*$  on this list and one value not on the list.

### 3. Fermi surface warping

In  $\text{Ti2201}$ , conduction is confined predominantly to the 2D copper–oxygen planes, resulting in a Fermi surface that is roughly cylindrical. However, some  $c$ -axis hopping from one plane to another does occur, indicative of a small, but non-zero, warping of the Fermi surface [8]. A convenient way to parametrize this warping is by expanding the local Fermi wavevector  $k_F$  in terms of cylindrical harmonics that respect the crystal symmetry. Since the  $\text{Ti2201}$  Fermi surface is centred on the X point (corner) of the Brillouin zone of a body-centred tetragonal structure, we can write [21, 28]

$$k_F(\phi, \kappa_z) = \sum_{\substack{\mu, \nu \geq 0 \\ \mu \bmod 4 = 0 \\ \nu \text{ even}}} k_{\mu, \nu} \cos \nu \kappa_z \cos \mu \phi + \sum_{\substack{\mu, \nu \geq 0 \\ \mu \bmod 4 = 2 \\ \nu \text{ odd}}} k_{\mu, \nu} \cos \nu \kappa_z \sin \mu \phi, \quad (18)$$

where  $\phi$  is the azimuthal angle of  $\mathbf{k}$ , and  $\kappa_z$  ranges from  $-\pi$  at the bottom of the Brillouin zone to  $\pi$  at the top of the Brillouin zone. It is found [8, 28–31] that only the lowest order



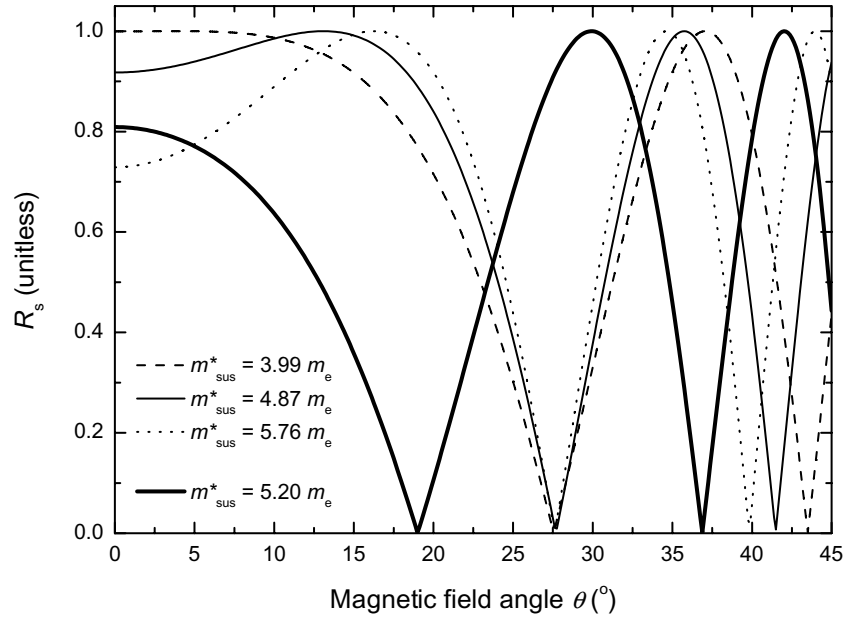


**Figure 1.** Angle dependence of the amplitude factor due to Fermi surface spin splitting,  $R_s$ , plotted for three values of  $m_{\text{sus}}^*$  ( $3.99m_e$ , dashed line;  $4.87m_e$ , solid line, and  $5.76m_e$ , dotted line) on the ‘magic list’ for a spin zero at  $\theta_0 = 27.6^\circ$  and one value ( $5.20m_e$ , heavy solid line) not on the list.

terms (illustrated in figure 2) are needed for describing the existing experimental data, so we can simplify equation (18) to

$$k_F(\phi, \kappa_z) = k_{0,0} \left( 1 + \frac{k_{4,0}}{k_{0,0}} \cos 4\phi \right) + k_{2,1} \cos \kappa_z \left( \sin 2\phi + \frac{k_{6,1}}{k_{2,1}} \sin 6\phi + \frac{k_{10,1}}{k_{2,1}} \sin 10\phi \right). \quad (19)$$

Having thus parametrized the Fermi surface geometry, we can calculate various physical properties in terms of  $k_{\mu,v}$ . For example, the zero-temperature resistive anisotropy of Tl2201 may be estimated as [21]

$$\frac{\rho_{0,c}}{\rho_{0,ab}} \approx \frac{8}{c^2 k_{2,1}^2 \left[ 1 + \left( \frac{k_{6,1}}{k_{2,1}} \right) + \left( \frac{k_{10,1}}{k_{2,1}} \right) \right]}, \quad (20)$$

where  $c$  is the  $c$ -axis lattice parameter. (Note that equation (20) is not exact, because it was derived under the assumption of circular in-plane Fermi surface cross-section, i.e.  $k_{4,0} = 0$ .)

As the Fermi surface of Tl2201 is close to being 2D, the usual extremal approximation [19] to determine the dHvA frequencies and amplitudes is insufficient. Instead we follow the approach of Bergemann *et al* [21] to obtain the oscillatory magnetization along the  $c$ -axis  $\tilde{M}_{\parallel c}$  by direct integration:

$$\tilde{M}_{\parallel c} \propto \int_0^{2\pi} \sin \left( \frac{\hbar a(\kappa_z)}{eB} \right) d\kappa_z, \quad (21)$$

where

$$a(\kappa_z) = \frac{1}{2 \cos \theta} \oint_0^{2\pi} k_F^2 [\phi, \kappa_z - \kappa_{\parallel}(\phi) \cos(\phi - \varphi) \tan \theta] d\phi \quad (22)$$

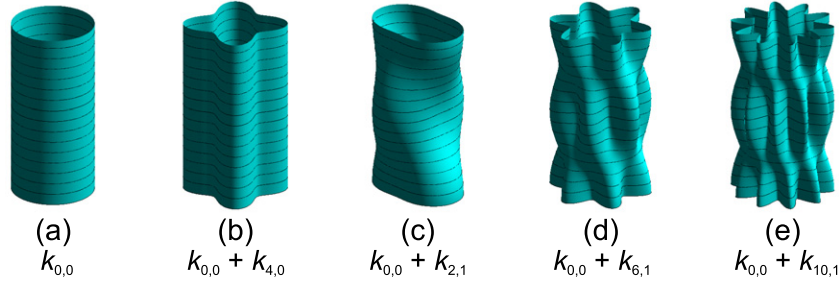


**Figure 2.** Diagrammatic representations of equation (18)  $(\mu, \nu)$  Fermi surface warping terms present in TI2201. In each case, warping terms not listed have had their  $k_{\mu,\nu} \equiv 0$ . (a)  $\mu = 0, \nu = 0$  only; (b)  $\mu = 0, \nu = 0$  and  $\mu = 4, \nu = 0$  only; (c)  $\mu = 0, \nu = 0$  and  $\mu = 2, \nu = 1$  only (also known as ‘the snake that swallowed a chain’ [21]); (d)  $\mu = 0, \nu = 0$  and  $\mu = 6, \nu = 1$  only; (e)  $\mu = 0, \nu = 0$  and  $\mu = 10, \nu = 1$  only. Note that, for illustrative purposes, the amount of warping shown in these cartoons is greatly exaggerated compared to the actual warping parametrized by the experimentally determined  $k_{\mu,\nu}$  in TI2201.

is the cross-sectional area of the Fermi surface perpendicular to the magnetic field direction that crosses the axis of the cylinder at  $\kappa_z$ .  $k_F$  is taken from equation (19), and

$$\kappa_{\parallel} = \frac{c}{2} (k_{0,0} + k_{4,0} \cos 4\phi) \quad (23)$$

is  $c/2$  times the in-plane Fermi wavevector.

Assuming that the in-plane Fermi surface cross-section is circular (i.e.  $k_{4,0} = 0$ ) and the warping parameters  $k_{\mu,1}$  are small compared to  $k_{0,0}$ , equations (22) and (21) may be integrated analytically. The result of such a treatment is a single quantum oscillation with a frequency given by equation (3) (with  $F_0 = \hbar k_{0,0}^2/2e$ ) and an overall amplitude modulation due to Fermi surface warping given by [21]

$$R_{\text{warp}}(B, \varphi, \theta) = \left| J_0 \left\{ 2\pi \sqrt{\frac{2\hbar F_0}{e}} \frac{k_{2,1}}{B \cos \theta} \left[ J_2 \left( c \sqrt{\frac{e F_0}{2\hbar}} \tan \theta \right) \sin 2\varphi \right. \right. \right. \\ \left. \left. + \frac{k_{6,1}}{k_{2,1}} J_6 \left( c \sqrt{\frac{e F_0}{2\hbar}} \tan \theta \right) \sin 6\varphi \right. \right. \\ \left. \left. + \frac{k_{10,1}}{k_{2,1}} J_{10} \left( c \sqrt{\frac{e F_0}{2\hbar}} \tan \theta \right) \sin 10\varphi \right] \right\} \right|, \quad (24)$$

in which  $J_{\mu}$  is the  $\mu$ th Bessel function of the first kind.

Like  $R_s$ ,  $R_{\text{warp}}$  can produce amplitude zeros at particular field angles  $\theta$  in a restricted range of field. However, the two effects can be easily distinguished, because the zeros due to warping occur at different  $\theta$  values for different values of  $\varphi$  and eventually disappear when  $\varphi \rightarrow 0$  (since  $\lim_{\varphi \rightarrow 0} R_{\text{warp}} = 1$ ), whereas spin zeros are fixed at the same values of  $\theta$  for all  $\varphi$ . Furthermore, because  $\lim_{\theta \rightarrow 0} R_{\text{warp}} = 1$ , the correction due to Fermi surface warping is weak for magnetic fields aligned near the  $c$ -axis, no matter what the value of  $\varphi$ .

#### 4. Experimental details

Tl2201 single crystals were grown using a self-flux method [32], and a range of sample dopings were obtained by annealing different crystals at different temperatures in flowing oxygen [32] and quenching quickly onto a copper block. The orientation and tetragonal structure of each single crystal were determined by x-ray diffraction. The samples exhibiting quantum oscillations have lattice parameters  $a = 3.86 \text{ \AA}$  and  $c = 23.2 \text{ \AA}$ . Crystals prepared in this way usually have  $7.5 \pm 2\%$  Cu on the Tl site [32].

For each sample, torque magnetization was measured using a piezo-resistive microcantilever<sup>4</sup>, balanced with a Wheatstone bridge circuit against a dummy microcantilever patterned onto the same substrate. Measurements were carried out with samples and cantilevers in liquid in a pumped  $^3\text{He}$  cryostat, using the 45 T hybrid magnet at the National High Magnetic Field Laboratory (NHMFL) in Tallahassee. The temperature of the cantilever was measured using the vapour pressure of  $^3\text{He}$  in which it was immersed. Great care was taken to reduce experimental noise levels as much as possible; doing so was essential in order to be able to observe the very weak quantum oscillations shown by our crystals.

More than 100 samples were pre-screened for purity [31], using criteria such as a low extrapolated residual  $c$ -axis resistivity, a high  $c$ -axis residual resistance ratio, magnitude of the transverse  $c$ -axis magnetoresistance and sharpness of the superconducting transition (measured via  $c$ -axis resistivity and superconducting quantum interference device magnetometry). Over 20 of the best of these samples, with  $T_c$  values ranging up to 60 K, were measured in high fields, including up to 70 T at the Laboratoire National des Champs Magnétiques Intenses in Toulouse. However, clear quantum oscillations were seen only in three crystals (and weak signals in one other crystal): two samples with  $T_c = 10 \text{ K}$ , labelled ‘Tl10Ka’ and ‘Tl10Kb’, and one sample with  $T_c = 26 \text{ K}$ , labelled ‘Tl26K’.

The fact that quantum oscillations were observed only in a small subset of the samples measured is due to the dephasing processes discussed in section 2. The exponential functional forms of  $R_D$ ,  $R_{\text{mos}}$  and  $R_{\text{dop}}$  (equations (10), (13) and (14)) lead to particularly strong damping, since they allow a small decrease in sample quality to reduce the oscillation amplitude by multiple orders of magnitude; these effects are especially severe in those compounds such as Tl2201 that have large Fermi surfaces. Thus, only the highest-quality crystals will exhibit quantum oscillations that are observable above the experimental noise floor.

Tl10Ka was mounted with the Cu–O bond direction parallel to the cantilever ( $\varphi \sim 0^\circ$ ), whereas Tl10Kb and Tl26K were mounted with  $\varphi \sim 45^\circ$ . The Tl26K cantilever was later rotated by  $45^\circ$  so that this sample was measured in both the  $\varphi \sim 0^\circ$  and the  $\varphi \sim 45^\circ$  orientations. Throughout this paper, data from Tl10Ka taken with  $\varphi \sim 0^\circ$  are shown as solid blue squares, data from Tl10Kb taken with  $\varphi \sim 45^\circ$  are shown as solid blue–green diamonds, data from Tl26K taken with  $\varphi \sim 0^\circ$  are shown as open red squares, data from Tl26K taken with  $\varphi \sim 45^\circ$  are shown as open red diamonds and theoretical fits and simulations are shown as black lines and symbols.

#### 5. Results

The high-field torque data for all three samples, taken at  $T = 0.4 \text{ K}$  with the magnetic field aligned close to the crystalline  $c$ -axis (i.e.  $\theta$  close to  $0^\circ$ ), are shown in the insets of figure 3, after

<sup>4</sup> Self-sensitive microcantilever; SII NanoTechnology Inc., Chuo-ku Tokyo, Japan; model number SSI-SS-ML-PRC120.

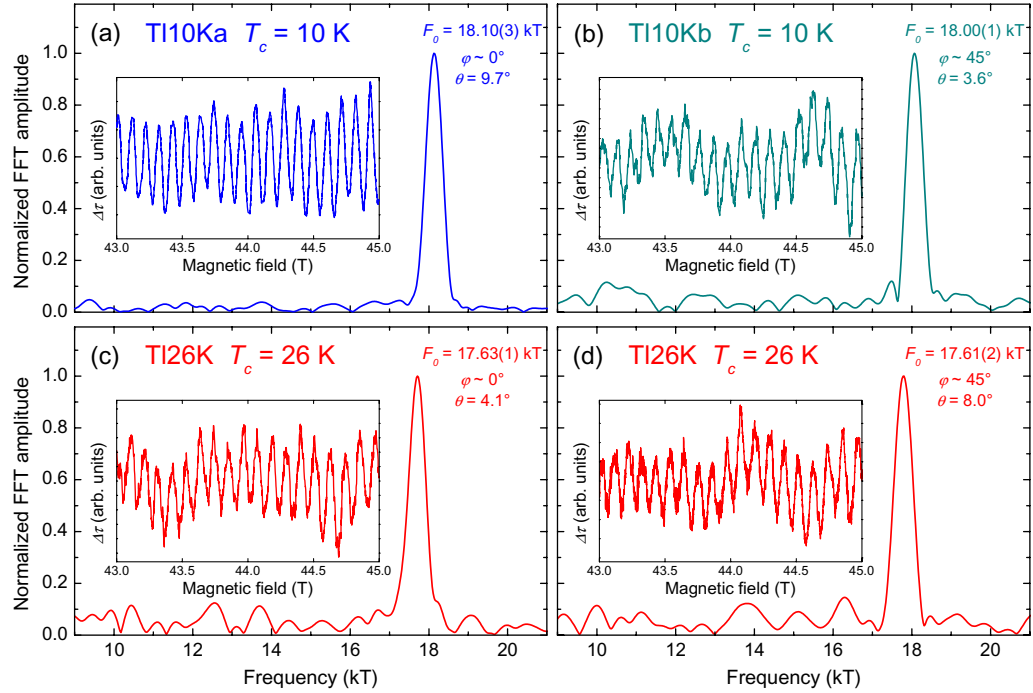


**Figure 3.** FFTs of torque data between 38 and 45 T (38.5 and 45 T for (d)) at  $T = 0.4$  K for (a) TI10Ka, (b) TI10Kb, (c) TI26K ( $\varphi \sim 0^\circ$  configuration) and (d) TI26K ( $\varphi \sim 45^\circ$  configuration). High-field portions of the corresponding background-subtracted raw data for each sample are shown in the insets.

third order polynomial background subtraction. Clear, high-frequency quantum oscillations are seen in all cases. We believe that the low-frequency background oscillations apparent in these traces are not intrinsic to our samples but arise from high-field magnetoresistance effects in the cantilevers themselves. Note that this cantilever magnetoresistance effect is not responsible for the low-frequency quantum oscillations seen in the underdoped cuprates [12], as in that case the oscillations are also measured in magnetotransport properties.

Fast Fourier transforms (FFTs) of the raw torque data are shown in the main panels of figure 3. Each sample shows a single sharp peak in the FFT spectrum (with width determined by the field range of measurement), centred at a lower frequency for TI26K than for TI10Ka or TI10Kb. As discussed in more detail below, this frequency shift with changing  $T_c$  confirms that the observed quantum oscillations originate from the same part of the sample exhibiting bulk superconductivity.

The temperature dependence of the quantum oscillation amplitude  $A(T)$  for TI10Ka, TI10Kb and TI26K is shown in figure 4. By fitting  $A(T)$  using the standard LK form of the temperature damping term  $R_T$  (equation (9)), we are able to determine the thermodynamic quasiparticle effective mass  $m_{\text{therm}}^*$  for each sample.  $A(T)$  is well fitted by the standard LK formula, indicating that any possible deviations from the usual thermal population factor (the Fermi function) arising from (marginal) non-Fermi-liquid effects [23, 24] are not apparent within the error bars of our measured data for temperatures above  $\sim 350$  mK, despite the presence of a significant  $T$ -linear resistivity at low temperatures [5, 33], to be discussed in more detail below.

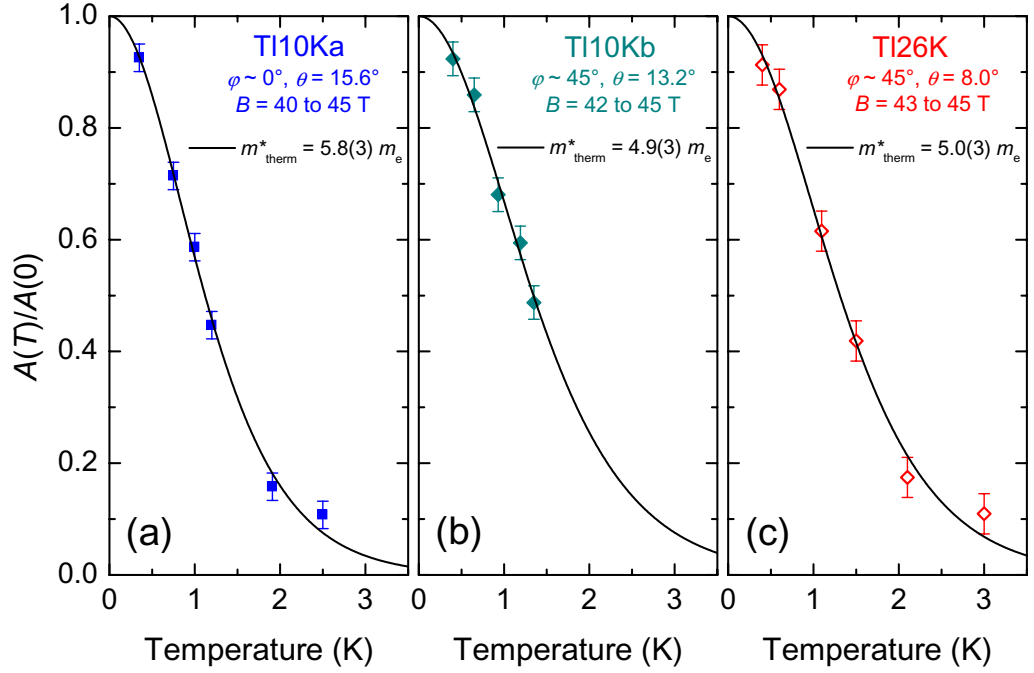


**Figure 4.** Temperature dependence of the oscillatory torque amplitudes  $A(T)$  for the samples (a) Tl10Ka (field range: 40–45 T), (b) Tl10Kb (field range: 42–45 T) and (c) Tl26K (field range: 43–45 T). Solid lines are fits to the Lifshitz-Kosevich form of  $R_T$  (equation (9)). For ease of comparison, all panels have been normalized to their respective zero-temperature fit values  $A(0)$ .

From our fits, we find that  $m_{\text{therm}}^* = 5.8(3)m_e$  for Tl10Ka ( $\varphi \sim 0^\circ$ ),  $m_{\text{therm}}^* = 4.9(3)m_e$  for Tl10Kb ( $\varphi \sim 45^\circ$ ) and  $m_{\text{therm}}^* = 5.0(3)m_e$  for Tl26K ( $\varphi \sim 45^\circ$ ). While the masses obtained for the two  $T_c = 10$  K samples are further apart than might be expected given the high quality of the fits, a deviation in temperature of the lowest temperature data points beyond our estimated error could influence the results.

To check for consistency and any field dependence of the dHvA mass (common in heavy Fermion systems, where  $m_{\text{therm}}^*$  is strongly enhanced by spin fluctuations), we compare our effective mass values to the zero-field electronic specific heat. For a 2D metal, the Sommerfeld coefficient is [34]

$$\gamma = \left( \frac{\pi k_B^2 N_A a^2}{3\hbar^2} \right) m_{\text{therm}}^*, \quad (25)$$

where  $N_A$  is Avogadro's constant. Taking the average  $m_{\text{therm}}^* = 5.2(4)m_e$ , we obtain  $\gamma = 7.6(6) \text{ mJ mol}^{-1} \text{ K}^{-2}$  in excellent agreement with the almost  $p$ -independent value of  $7(1) \text{ mJ mol}^{-1} \text{ K}^{-2}$  found from direct measurement of polycrystalline Tl2201 [35].

Comparison with the band mass  $m_b \sim 1.7m_e$ , given by density functional theory band-structure calculations (see section 6), reveals a significant enhancement due to electron correlation effects ( $m_{\text{therm}}^*/m_b \approx 3$ ) that is constant (within our uncertainty) up to at least  $\sim 0.3 T_c^{\text{max}}$ . ARPES measurements showed that the band energies of Tl2201 ( $T_c = 30$  K) [37] are renormalized by a similar factor over a large energy range of the order of several eV. In fact, using the tight binding parametrization of the ARPES data given in [36], we calculate an

orbitally averaged mass  $m_{\text{ARPES}}^* = \frac{\hbar^2}{2\pi} \frac{\partial A}{\partial \varepsilon} = 6.6 m_e$ , which is  $\sim 20\%$  larger than our measured dHvA mass. This implies that the renormalization predominantly arises from correlation-induced band-narrowing and that any further renormalization close to the Fermi level  $E_F$  from interaction with low-energy boson modes is minimal.

Having pinned down the  $R_T$  damping term by looking at the temperature dependence of the quantum oscillation amplitude  $A(T)$ , it is possible to learn about the exponential damping terms  $R_D$ ,  $R_{\text{mos}}$  and  $R_{\text{dop}}$  by fitting the field dependence of the amplitude  $A(B)$ . Specifically, if we define

$$A_{\text{reduced}}(B) \equiv A(B) / R_{\text{torque}}(B) R_T(B) \quad (26)$$

and measure long field sweeps at magnetic field angles  $\theta$  close to the  $c$ -axis, where  $R_{\text{warp}} \sim 1$ , then

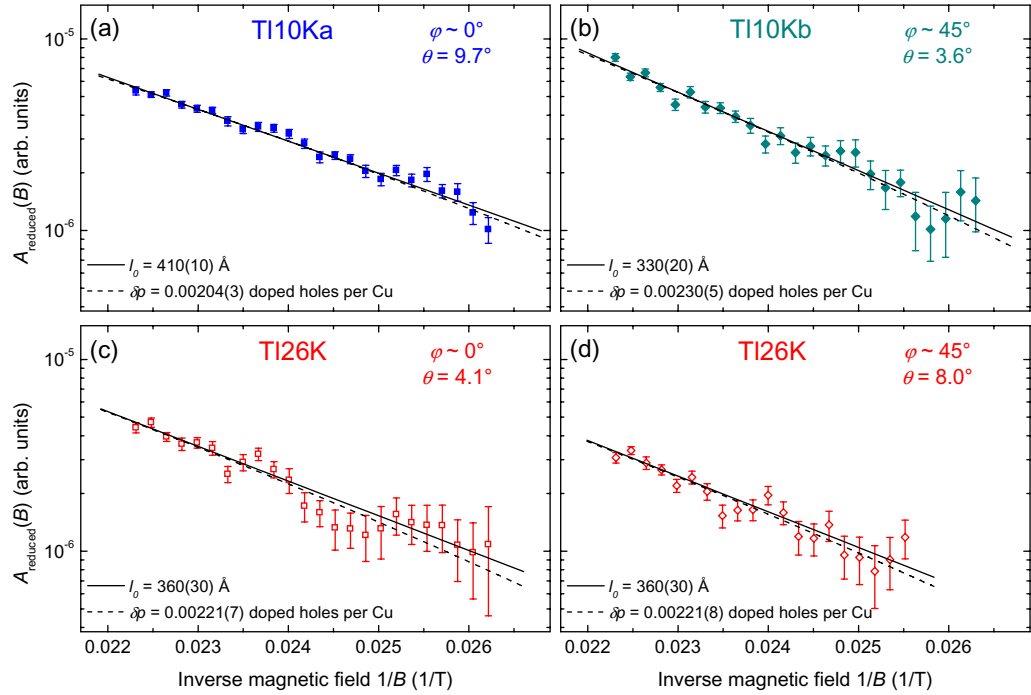
$$\begin{aligned} \ln A_{\text{reduced}}(1/B) &\approx \ln[A_0 R_D(1/B) R_{\text{mos}}(1/B) R_{\text{dop}}(1/B)] \\ &\approx \ln(A_0) - \left[ \pi \sqrt{\frac{2\hbar F_0}{e}} \frac{1}{\ell_0 \cos \theta} \right] \left( \frac{1}{B} \right) \\ &\quad - \left[ \pi F_0 \left( \frac{\sin \theta}{\cos^2 \theta} \right) \delta\theta + \frac{\pi^2 \hbar \delta p}{a^2 e \cos \theta} \right]^2 \left( \frac{1}{B} \right)^2. \end{aligned} \quad (27)$$

Figure 5 shows experimental  $A_{\text{reduced}}(B)$  data extracted from the magnetic field sweeps shown in figure 3. A high-pass FFT filter was applied to the raw oscillation data to remove the extrinsic low-frequency background oscillation; then  $A(B)$  was extracted by directly fitting the data in three-period segments to a sine function that is periodic in  $1/B$ . For each data point, we convert  $A(B)$  into  $A_{\text{reduced}}(B)$  using equation (26) and the experimentally determined masses  $m_{\text{therm}}^*$  obtained from the fits shown in figure 4.

Our error bars and field range of measurement (the oscillations are lost into the noise floor at lower fields) make it difficult to disentangle the influences of  $R_D$ ,  $R_{\text{mos}}$  and  $R_{\text{dop}}$  on the field dependence of  $A_{\text{reduced}}(B)$ . However, limiting values may be obtained by considering the effect of each damping term in the absence of the other two. Thus, for example, by assuming that all damping of  $A_{\text{reduced}}(B)$  comes from impurity scattering (i.e.  $\delta p \equiv \delta\theta \equiv 0$ ), error weighted fits to our data (solid lines in figure 5) yield lower limit mean free path values of  $\ell_0 = 410(10)$  Å for Tl10Ka,  $\ell_0 = 330(20)$  Å for Tl10Kb,  $\ell_0 = 360(30)$  Å for Tl26K measured with  $\varphi \sim 0^\circ$  and  $\ell_0 = 360(30)$  Å for Tl26K measured with  $\varphi \sim 45^\circ$ . Although in some sense self-selection is responsible for the small range of measured  $\ell_0$  values (reducing  $\ell_0$  by 1.3 would decrease the strength of the dHvA signal by a factor of 10), the fact that we could find samples with sufficiently long  $\ell_0$  to allow the observation of quantum oscillations shows that no intrinsic quasiparticle decoherence beyond this scattering level arises as the doping is decreased towards  $T_c^{\text{max}}$ . For example, if part of the electron orbit started to become incoherent due to the onset of the pseudogap, this would provide a fundamental limitation.

Similarly, by assuming that all damping comes from doping inhomogeneity (i.e.  $\ell_0 \equiv \infty$  and  $\delta\theta \equiv 0$ ), error-weighted fits to our data (dashed lines in figure 5) yield upper limit doping spread values of  $\delta p = 0.00204(3)$  doped holes per in-plane Cu atom for Tl10Ka,  $\delta p = 0.00230(5)$  holes for Tl10Kb,  $\delta p = 0.00221(7)$  holes for Tl26K measured with  $\varphi \sim 0^\circ$  and  $\delta p = 0.00221(8)$  holes for Tl26K measured with  $\varphi \sim 45^\circ$ . This is an important result as it





**Figure 5.** Logarithmic plots of the reduced oscillation amplitude  $A_{\text{reduced}}(B) \equiv A(B)/R_{\text{torque}}(B)R_T(B)$  versus inverse field  $1/B$ , for the data shown in figure 3. A high-pass FFT filter was applied to the raw oscillation data to remove the extrinsic low-frequency background oscillation; then  $A(B)$  was extracted by directly fitting the data in three-period segments to a sine function that is periodic in  $1/B$ . Lines are error-weighted fits to equation (27) in which all exponential damping is assumed to come from either impurity scattering (solid, with  $\delta p \equiv \delta \theta \equiv 0$ ) or doping inhomogeneity (dashed, with  $\ell_0 \equiv \infty$  and  $\delta \theta \equiv 0$ ).

demonstrates that the doping distribution in overdoped TI2201 is negligibly small on the length scale of  $\ell_0 \gtrsim 400 \text{ \AA}$ . Indeed, were  $\ell_0$  a factor of 2 smaller or  $\delta p$  a factor of 2 larger, the overall quantum oscillation amplitude would be reduced by over four orders of magnitude, rendering the oscillations unobservable within our current experimental noise floor.

From another perspective, the fact that we observe quantum oscillations at all implies that the combined damping from all types of sample inhomogeneity is minimal over a length scale of the order of the cyclotron radius  $r_c$

$$r_c = \frac{\hbar k_F}{eB} \approx \sqrt{\frac{2F_0 \hbar}{e}} \frac{1}{B}. \quad (28)$$

For  $F_0 = 18 \text{ kT}$  and  $B = 40 \text{ T}$ ,  $r_c \sim 1200 \text{ \AA}$ .

In order to characterize the fine details of the  $\text{CuO}_2$  plane-derived Fermi surface shape in TI2201 and how this shape changes with doping, we have performed a full angle dependence study of the quantum oscillations. For the  $T_c = 10 \text{ K}$  and  $T_c = 26 \text{ K}$  samples, respectively, figures 6 and 7 show the field angle dependence of the dHvA frequency  $F(\theta)$  for both the  $\varphi$  directions (panel (a)), the dHvA amplitude  $A(\theta)$  for  $\varphi \sim 0^\circ$  (panel (b)) and the dHvA amplitude



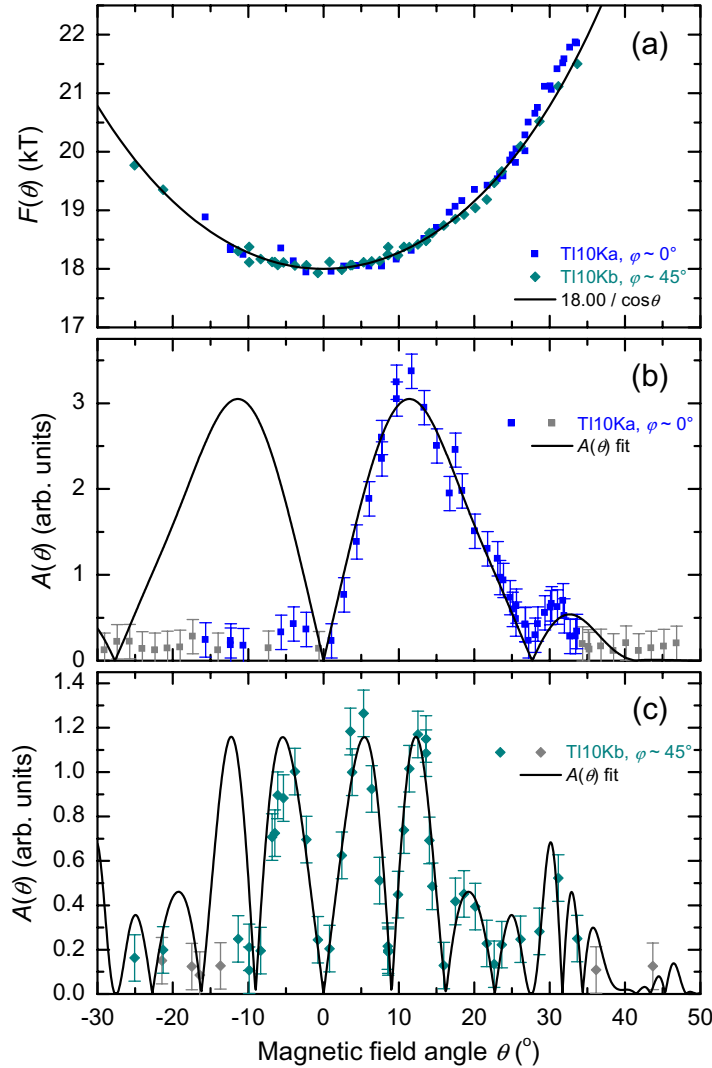


**Figure 6.** Quantum oscillation dependence on polar magnetic field angle  $\theta$  for TI10Ka and TI10Kb, extracted from the highest peak of the FFT spectrum in a 15–30 kT window at each angle. Data points at which the signal has fallen into the noise have been removed from (a) and are shown in grey (b) and (c). (a) Oscillation frequency  $F(\theta)$  for both samples (i.e. both  $\varphi$  orientations), with a fit of equation (3) to the TI10Kb  $\varphi \sim 45^\circ$  data (not including noise points) shown as a solid line. (b) Oscillation amplitude  $A(\theta)$  for TI10Ka in the  $\varphi \sim 0^\circ$  orientation, along with a fit to equation (5) (for  $\theta \geq 0^\circ$  only), using the analytical form of  $R_{\text{warp}}$  given by equation (24),  $R_D$  given by equation (29), and fitting parameters shown in table 1. (c) Oscillation amplitude  $A(\theta)$  for TI10Kb in the  $\varphi \sim 45^\circ$  orientation, along with a fit to equation (5) (for  $\theta \geq 0^\circ$  only), using the analytical form of  $R_{\text{warp}}$  given by equation (24),  $R_D$  given by equation (29) and fitting parameters shown in table 1. Note the strong asymmetry seen particularly in (b), discussed in the text.

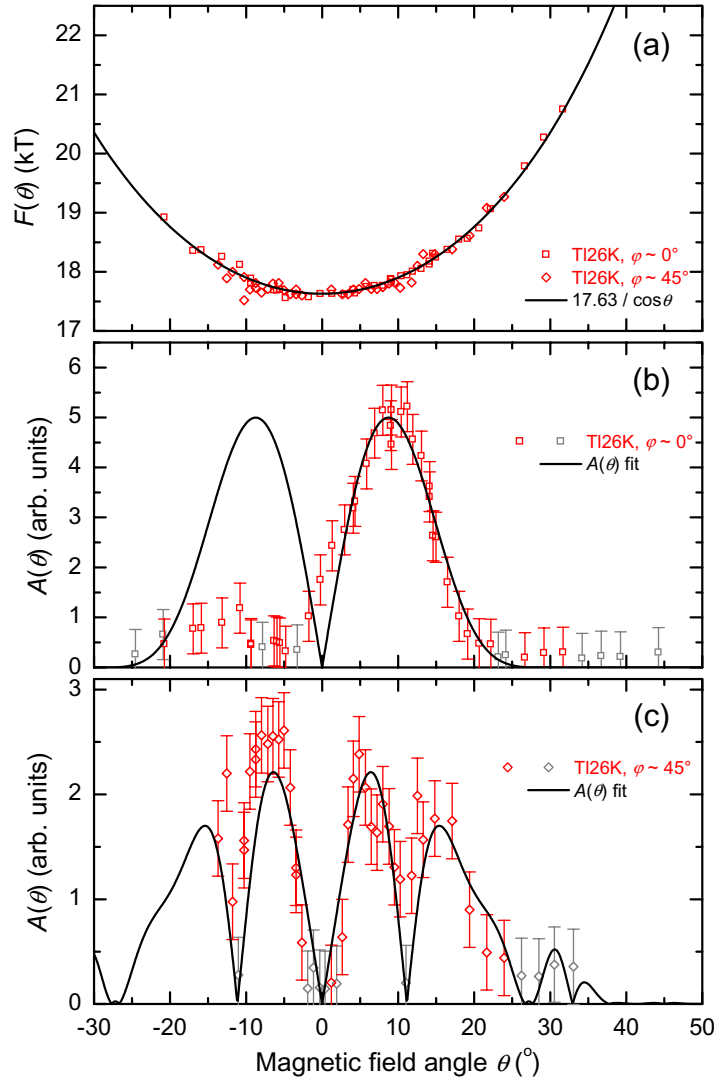


**Figure 7.** Quantum oscillation dependence on polar magnetic field angle  $\theta$  for TI26K, extracted from the highest peak of the FFT spectrum in a 15–30 kT window at each angle. Data points at which the signal has fallen into the noise have been removed from (a) and are shown in grey (b) and (c). (a) Oscillation frequency  $F(\theta)$  for both  $\varphi$  orientations, with a fit of equation (3) to the TI26K  $\varphi \sim 0^\circ$  data (not including noise points) shown as a solid line. (b) Oscillation amplitude  $A(\theta)$  for TI26K in the  $\varphi \sim 0^\circ$  orientation, along with a fit to equation (5) (for  $\theta \geq 0^\circ$  only), using the analytical form of  $R_{\text{warp}}$  given by equation (24),  $R_D$  given by equation (29) and fitting parameters shown in table 1. (c) Oscillation amplitude  $A(\theta)$  for TI26K in the  $\varphi \sim 45^\circ$  orientation, along with a fit to equation (5) (for  $\theta \geq 0^\circ$  only), using the analytical form of  $R_{\text{warp}}$  given by equation (24),  $R_D$  given by equation (29) and fitting parameters shown in table 1. Note the strong asymmetry seen particularly in (b), discussed in the text.

**Table 1.** Fitting parameters used to generate the  $A(\theta)$  fit curves shown in panels (b) and (c) of figures 6 and 7.

Parameter	Units	Tl10Ka, $\varphi \sim 0^\circ$	Tl10Kb, $\varphi \sim 45^\circ$	Tl26K, $\varphi \sim 0^\circ$	Tl26K, $\varphi \sim 45^\circ$
$\varphi^a$	deg	6 <sup>a</sup>	45	0	45
$A_0^b$	arb.	$3.8(1) \times 10^{-3}$	$18.6(7) \times 10^{-3}$	$23.0(7) \times 10^{-3}$	$10.0(8) \times 10^{-3}$
Temperature	K	0.45(5)	0.45(5)	0.45(5)	0.45(5)
$m_{\text{therm}}^*$	$m_e$	5.8(2)	4.9(2)	5.0(2)	5.0(2)
$m_{\text{sus}}^*$	$m_e$	4.87	4.87	4.87	4.87
$F_0$	kT	18.10(3)	18.00(1)	17.63(1)	17.61(2)
$\ell_0$	Å	410(10)	330(20)	360(30)	360(30)
$n^b$	–	1.58(6)	0.92(9)	4.5(1)	1.6(3)
$\delta p^c$	holes	0	0	0	0
$\delta \theta^c$	deg	0	0	0	0
c	Å	23.2	23.2	23.2	23.2
$k_{2,1}$ (see footnote 5)	Å <sup>-1</sup>	−0.00170(5)	−0.00170(5)	−0.00125(5)	−0.00125(5)
$k_{6,1}/k_{21}$	–	0.71	0.71	0.62	0.62
$k_{10,1}/k_{21}$	–	−0.25	−0.25	−0.39	−0.39
Field range	tesla	42–44	42–45	42–45	43–45
$B_{\text{mid}}$	tesla	42.977	43.448	43.448	43.977

<sup>a</sup>Samples were aligned on the cantilevers by x-ray diffraction, and cantilevers were aligned on the experimental probe by the eye; the detailed shape of  $A(\theta)$  for the nominally  $\varphi \sim 0^\circ$  Tl10Ka sample is best fitted with  $\varphi = 6^\circ$ .

<sup>b</sup>As described in the text, the final least-squares fits shown in figures 6 and 7 have only  $A_0$  and  $n$  as free fitting parameters.

<sup>c</sup>Since the effects of  $R_D$ ,  $R_{\text{mos}}$  and  $R_{\text{dop}}$  are similar,  $\delta p$  and  $\delta \theta$  were set to 0 to constrain the fitting.

$A(\theta)$  for  $\varphi \sim 45^\circ$  (panel (c)). At each  $\theta$  angle,  $F(\theta)$  and  $A(\theta)$  were extracted from the highest peak in the FFT within a fairly broad window (15–30 kT); thus, at angles where the quantum oscillation amplitude is so low that the signal has fallen into the noise, these data points (shown in grey in figures 6 and 7) represent the highest peaks of the noise spectrum at those particular angles and are useful for getting a sense of the overall noise floor of the experiment.

Fitting the frequency angle dependence  $F(\theta)$  of the  $T_c = 10$  K samples (figure 6(a)) to the quasi-2D, roughly cylindrical Fermi surface form ( $= F_0/\cos \theta$ ), we obtain fundamental frequencies  $F_0$  of 18.10(3) and 18.00(1) kT for Tl10Ka and Tl10Kb, respectively, in agreement with a previous study in pulsed fields [15]. Similarly, for the  $T_c = 26$  K sample Tl26K (figure 7(a)), we obtain fundamental frequencies  $F_0$  of 17.63(1) kT for  $\varphi \sim 0^\circ$  and 17.61(2) kT for  $\varphi \sim 45^\circ$ . Since  $F_0$  is directly related to the extremal cross-sectional area  $\mathcal{A}_{\text{ext}}$  of the Fermi surface via the Onsager relationship (equation (1)), we find that the radius  $k_{0,0}$  of the roughly cylindrical Fermi surface is 0.7416(6) Å<sup>-1</sup> for Tl10Ka, 0.7396(2) Å<sup>-1</sup> for Tl10Kb, 0.7319(2) Å<sup>-1</sup> for Tl26K ( $\varphi \sim 0^\circ$ ) and 0.7315(4) Å<sup>-1</sup> for Tl26K ( $\varphi \sim 45^\circ$ ). Furthermore, from equation (15), we obtain hole dopings  $p$  of 0.304(2), 0.2970(7), 0.2703(7) and 0.269(1)

<sup>5</sup> Note that the sign of  $k_{2,1}$  cannot be determined experimentally by either dHvA or ADMR and has thus been chosen to be negative to match that found by fitting band-structure calculations (see section 6).

holes per in-plane Cu atom, respectively, for Tl10Ka, Tl10Kb, Tl26K ( $\varphi \sim 0^\circ$ ) and Tl26K ( $\varphi \sim 45^\circ$ ). These values are consistent with those originally determined by ADMR ( $k_{0,0} = 0.745(8) \text{ \AA}^{-1}$ ) [8] and the measured zero-temperature Hall number  $n_H(0) = 1.28(6)$  per Cu for a  $T_c = 15 \text{ K}$  sample [33].

Moving on to the angle dependence of the quantum oscillation amplitude  $A(\theta)$  (panels (b) and (c) of figures 6 and 7), one can immediately notice that for both dopings, the data sets taken in the  $\varphi \sim 45^\circ$  orientation go to zero at many more angles than those taken with  $\varphi \sim 0^\circ$ . In Tl10Ka ( $\varphi \sim 0^\circ$ ), beyond the amplitude zero at  $\theta = 0^\circ$  caused by  $R_{\text{torque}}$ , only one amplitude zero is seen, at  $\theta_0 = 27.6(1.0)^\circ$ . Since zeros due to warping disappear as  $\varphi \rightarrow 0^\circ$ , this zero must arise from the spin-splitting term  $R_s$ . Unfortunately, no additional spin zeros are visible for  $\varphi \sim 0^\circ$ , so while we know that the susceptibility mass  $m_{\text{sus}}^*$  lies on the ‘magic list’ written at the end of section 2, it cannot be specified more precisely. (However, we can truncate the list at a maximum value of  $m_{\text{sus}}^* = 7.53m_e$  because higher values cause additional zeros at  $\theta < 27^\circ$ , which are ruled out experimentally.) Since  $m_{\text{sus}}^* = 4.87m_e$  is close to the experimentally determined values of  $m_{\text{therm}}^*$  and best matches the overall  $\theta$  dependence of both the Tl10Ka ( $\varphi \sim 0^\circ$ ) and Tl10Kb ( $\varphi \sim 45^\circ$ ) data, we use this value for our fits ( $m_{\text{sus}}^* = 3.99m_e$  and  $5.76m_e$  also give good fits and are close to  $m_{\text{therm}}^*$ ). For a given value on the magic list, the experimental error of  $\sim \pm 1^\circ$  in  $\theta_0$  corresponds to an error of approximately  $0.04m_e$  in  $m_{\text{sus}}^*$ . While no spin zeros can be seen in the Tl26K  $\varphi \sim 0^\circ$  data, the overall amplitude  $\theta$  dependence is consistent with the presence of a zero near  $\theta_0 = 27.6(1.0)^\circ$  and so we assume that  $m_{\text{sus}}^* = 4.87m_e$  for the Tl26K fits as well.

For  $\varphi \sim 45^\circ$ , the minima observed below  $\theta = 25^\circ$  are caused by  $R_{\text{warp}}$  and specifically determined by the value of  $k_{2,1}$ , the dominant component of the  $c$ -axis warping and a parameter that cannot be determined directly by ADMR or ARPES experiments. We varied  $k_{2,1}$  until the first amplitude zero from  $R_{\text{warp}}$  matched the angle of that seen in the data; for the same  $k_{2,1}$  value, the higher-angle warping zeros seen in the Tl10Kb data automatically matched those predicted by  $R_{\text{warp}}$  as well. Our data show that  $k_{21} = -0.00170(5)$  and  $-0.00125(5) \text{ \AA}^{-1}$  for  $T_c = 10 \text{ K}$  and  $26 \text{ K}$ , respectively<sup>6</sup>, corresponding to a resistivity anisotropy  $\rho_c/\rho_{ab}$  of  $3.3(2) \times 10^3$  and  $6.2(5) \times 10^3$  (estimated using equation (20), assuming isotropic scattering and including  $k_{6,1}/k_{2,1}$  and  $k_{10,1}/k_{2,1}$  from previous ADMR measurements [8, 30], as listed in table 1). These values are in reasonable quantitative agreement with reported anisotropies ( $\rho_c/\rho_{ab} = 2.5 \times 10^3$  at  $T = 30 \text{ K}$ ) for Tl2201 single crystals with similar  $T_c$  values [38]. The rise in anisotropy as  $T_c^{\text{max}}$  is approached derived from our data is, however, significantly steeper than observed in resistivity measurements [39]. This could result from experimental difficulties in resistive measurements of highly anisotropic crystals or a strong anisotropy in the scattering rate for the  $c$ -axis versus in-plane transport.

The overall broad angle dependence of the amplitude, which damps out with increasing  $\theta$ , is difficult to model precisely as it depends on detailed knowledge of the  $\theta, \varphi$  dependence of the scattering rate, mosaic spread and doping inhomogeneity in the portion of the sample from which quantum oscillations arise. In particular, we observed a strong asymmetry in the angular dependence for  $\varphi \sim 0^\circ$  (evident in figures 6 and 7). Some asymmetry has been seen by us in other systems measured using the same microcantilevers and is not understood. In the present study, this asymmetry is much weaker for  $\varphi \sim 45^\circ$ , and importantly, the positions of the minima, which determine  $k_{2,1}$ , are symmetric with respect to  $\pm\theta$ .

<sup>6</sup> Note that the sign of  $k_{2,1}$  cannot be determined experimentally by either dHvA or ADMR and has thus been chosen to be negative to match that found by fitting band-structure calculations (see section 6).

Nevertheless, we have attempted to quantify the broad  $\theta$  dependence of the oscillation amplitude by fitting  $A(\theta)$  ( $\theta \geq 0^\circ$ ) to the full form of equation (5). Since the angle dependences of  $R_D$ ,  $R_{\text{mos}}$  and  $R_{\text{dop}}$  are similar to each other and therefore difficult to disentangle,  $\delta\theta$  and  $\delta p$  were set to 0 in order to allow fitting parameters to be constrained. Furthermore, given the lower limits of the scattering mean free path  $\ell_0$  determined from the low-angle  $A_{\text{reduced}}(B)$  fits shown in figure 5, the oscillation amplitudes  $A(\theta)$  are damped out much more quickly with increasing  $\theta$  than predicted by the quasi-2D, isotropic- $\ell$  version of  $R_D$  from equation (10) (especially when  $\varphi \sim 0^\circ$ ). In order to accommodate the unknown  $\theta, \varphi$  dependence of  $\ell$  in the simplest manner possible, we modify equation (10) to

$$R_D(B, \theta) = \exp \left\{ -\pi \sqrt{\frac{2\hbar F_0}{e}} \frac{1}{\ell_0 B (\cos \theta)^n} \right\}, \quad (29)$$

where the  $\ell_0$  values are fixed at those determined from  $A_{\text{reduced}}(B)$  and  $n$  is a free fitting parameter. Using the formula for  $R_D$  (equation (29)), the analytical form of  $R_{\text{warp}}$  given by equation (24) and parameters shown in table 1, we generate least-squares fits to the  $\theta \geq 0^\circ$  data shown in figures 6 and 7, with the fits shown as lines in the aforementioned figures. In these fits, only  $A_0$  and  $n$  are free parameters, with the values of the other parameters deduced as above. The magnetic field strength  $B$  used in equation (5) and in the equations for the damping terms is taken to be the mid-point  $B_{\text{mid}}$  of the field sweep range in  $1/B$ . Also, for completeness, higher order warping terms  $k_{6,1}/k_{2,1}$  and  $k_{10,1}/k_{2,1}$  determined by previous ADMR studies of overdoped Tl2201 crystals from the same crystal growth batch [8, 31] were included in the fits, although as discussed below, our quantum oscillation data are not very sensitive to these particular warping parameters.

Since (i) the analytical form of  $R_{\text{warp}}$  shown in equation (24) was derived under the assumption that  $k_{4,0} = 0$ , but we know from the previous ADMR measurements of overdoped Tl2201 that  $k_{4,0}/k_{0,0} = -0.032$  [8, 31]; and (ii) the methodology for deriving equation (24) [21] has recently come into question [40], we have endeavoured to confirm our results numerically. To this end, we have directly computed the full oscillatory magnetization along the  $c$ -axis from equations (19), (21), (22) and (23) at 1000 magnetic field values per tesla within the field ranges measured experimentally, then extracted  $A(\theta)$  using the same treatment as the one we applied to the experimental data (i.e. from the peak in the FFT). In these numerical simulations, spin-splitting was explicitly taken into account by calculating and summing different  $\tilde{M}_{\parallel c, \uparrow \downarrow}$  for the majority-spin and minority-spin Fermi surface sheets at each field value; the other damping factors (including  $R_{\text{torque}}$ , which converts the calculated  $\tilde{M}_{\parallel c}$  to torque) were also applied directly at each field. Unless indicated otherwise, the same parameters as the analytical fits (shown in table 1) were used for the simulations.

A comparison between analytical fits and numerical simulations for each doping/ $\varphi$  combination is shown in figure 8. Analytical fits (solid lines) are the same as those in panels (b) and (c) of figures 6 and 7. Two types of numerical simulation were run: one with the full parametrized Fermi surface, including  $k_{0,0}$ ,  $k_{4,0}$ ,  $k_{2,1}$ ,  $k_{6,1}$  and  $k_{10,1}$  (open circles), and the other including only  $k_{0,0}$  and  $k_{2,1}$  (+ symbols). From these comparisons, we can clearly see that (i) the results are nearly identical whether or not  $k_{4,0}$  is included and whether or not the analytical expression was used; and (ii) the effects of  $k_{6,1}$  and  $k_{10,1}$  are only apparent at high angles  $\theta \gtrsim 25^\circ$ , where we have few experimental data points.

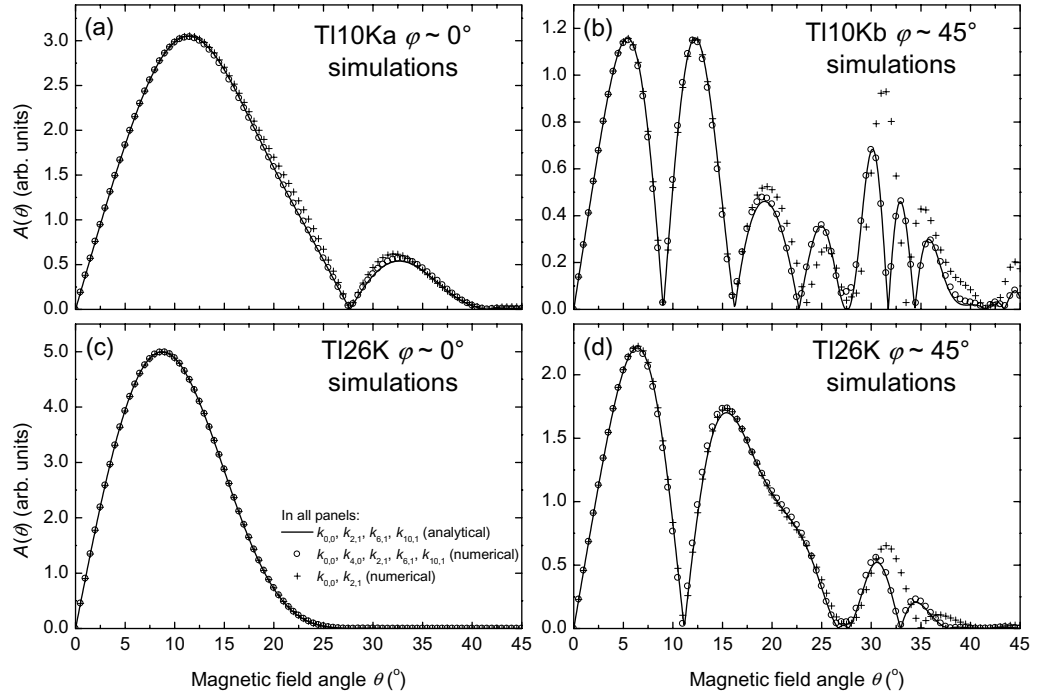


**Figure 8.** Comparison (for all four doping/ $\varphi$  combinations) of the amplitude angle dependence  $A(\theta)$  obtained using the analytical equation (24) with  $k_{0,0}$ ,  $k_{2,1}$ ,  $k_{6,1}$  and  $k_{10,1}$  (solid lines); numerical simulations of equation (21) with  $k_{0,0}$ ,  $k_{2,1}$ ,  $k_{6,1}$  and  $k_{10,1}$  (circles); and numerical simulations of equation (21) with  $k_{0,0}$  and  $k_{2,1}$  only (+ symbols). All other parameters are taken from table 1.

## 6. Band structure

Now that we have an accurate experimental determination of the Fermi surface of TI2201, it is instructive to compare this in detail to density functional theory (DFT) band-structure calculations. To do this, we have calculated the band structure of TI2201 using the Wien2K package [41], which is an implementation of a full-potential, augmented plane-wave plus local orbital scheme (APWlo). We used a generalized gradient approximation form for the exchange correlation potential [42] and  $10^4$   $k$ -points for convergence. The structure used was based on that determined by Liu *et al* [43], but with the Tl and O(3) atoms moved to the symmetry points with full occupancy: Tl (0.5, 0.5, 0.203), Ba (0, 0, 0.0842), Cu (0.5, 0.5, 0), O(1) (0, 0.5, 0), O(2) (0.5, 0.5, 0.1168), O(3) (0.5, 0.5, 0.289), space group 139 (I4/mmm), lattice constants  $a = 3.861$  Å,  $c = 23.133$  Å.

The Fermi surface resulting from this calculation is similar to that reported previously [44] with two sheets: one large hole-like quasi-2D sheet derived from the  $\text{CuO}_2$  planes (containing 1.05 holes) and a small electron-like spherical sheet derived from the Tl–O layers (containing 0.05 electron). The total volume of the Fermi surface corresponds to half-filling, i.e. one electron per Cu atom. Our samples are overdoped (because of Tl deficiency and excess oxygen). A simple way to simulate this is to rigidly shift the energy of the bands until the experimental doping level is achieved. An alternative, more accurate approach is to employ the virtual crystal approximation (VCA) where the doping is achieved by replacing the Tl atom with a virtual



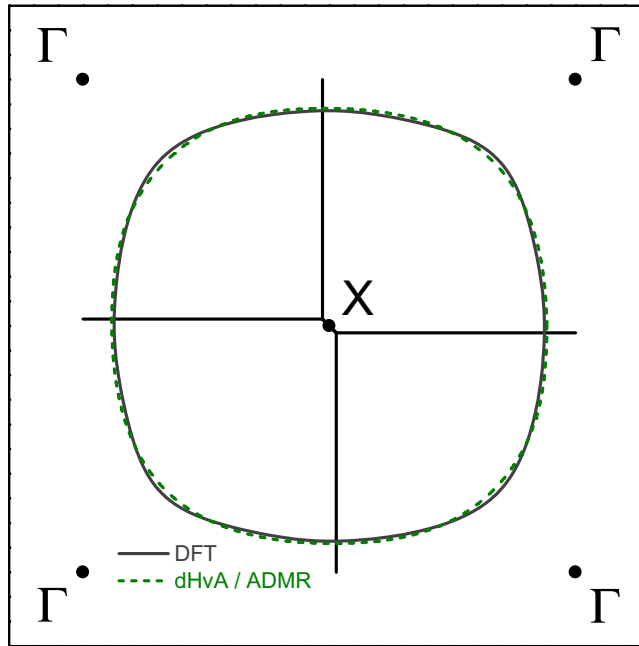


**Figure 9.** Comparison of the (001) cross-section of the Fermi surface of Tl2201 at  $k_z = 0$  calculated by DFT band structure with that derived from dHvA and ADMR experiments.

atom of non-integral charge [45]. With this approach, the Tl–O band moves much more rapidly than the  $\text{CuO}_2$  band [45]. In order to get a doping of  $p = 0.31$  we need to reduce the charge per Tl site from 81 to 80.846.

A (001) cross-section of the Fermi surface at  $k_z = 0$  is compared in figure 9 to the same cross-section calculated using the parameters derived from the present experiments. For this calculation a very dense mesh of  $1.6 \times 10^5$   $k$ -points was used in the 2D grid. The level of agreement is very good. We note that a previous calculation of Platé *et al* [36, 37] predicted a much more square Fermi surface than that found experimentally. This is presumably a result of the tight-binding linear muffin-tin orbital (TBLMTO) method used, which is evidently less accurate than the present full-potential APWlo calculation for the case of Tl2201.

To make a more detailed comparison between the DFT calculation and experiment, we fitted  $k_F(\phi, k_z = 0)$  to the harmonic expansion given in equation (18) (figure 10(a)). To get a fit within the numerical noise level of the calculation, we need to include four cosine warping terms ( $k_{4,0}, k_{8,0}, k_{12,0}, k_{16,0}$ ), whereas to fit the ADMR data just the  $k_{4,0}$  parameter was needed. However, the small magnitude of these extra terms ( $k_{4,0} \simeq 5k_{8,0} \simeq 35k_{12,0} \simeq 100k_{16,0}$ ) means that they are difficult to detect experimentally. For example, the experimental error in  $k_{4,0}$  is the same order of magnitude as  $k_{8,0}$ . The residuals after subtracting a fit with just the cosine terms are shown in figure 10(b). These residuals correspond to the  $c$ -axis warping of the Fermi surface—the cross-section at  $k_z = \pi/2$  does not contain any sine term (by symmetry) and is fitted within the noise by the cosine terms alone. The sine terms needed to fit these residuals within the numerical noise are exactly the same components  $k_{2,1}, k_{6,1}$  and  $k_{10,1}$  needed to fit the ADMR data. The fact that this was determined experimentally from the analysis of ADMR measurements [8] prior to these calculations is a testament to the robustness of the



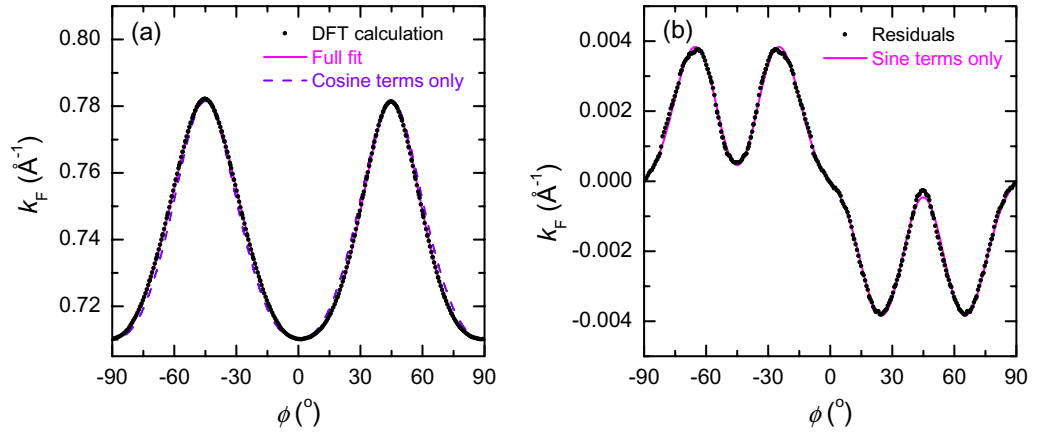


**Figure 10.** (a) DFT VCA calculation of  $k_F(\phi)$  at  $k_z = 0$ . The solid line is the full fit using both the cosine and sine terms described in the text (see table 2). The dashed line is a fit using just the cosine terms. The residuals from this latter fit are shown in (b) and are fitted using the sine terms listed in table 2.

**Table 2.** Fitting parameters from the DFT VCA band-structure calculation compared to parameters derived from the present dHvA study ( $k_{0,0}$  and  $k_{2,1}$ ) and ADMR measurements ( $k_{4,0}$ ,  $k_{6,1}$ ,  $k_{10,1}$ ) for the  $T_c = 10$  K sample. The units of  $k_{0,0}$  and  $k_{2,1}$  are  $\text{\AA}^{-1}$ .

	$k_{0,0}$	$\frac{k_{4,0}}{k_{0,0}}$	$\frac{k_{8,0}}{k_{0,0}}$	$\frac{k_{12,0}}{k_{0,0}}$	$\frac{k_{16,0}}{k_{0,0}}$	$k_{2,1}$ (see footnote 7)	$\frac{k_{6,1}}{k_{2,1}}$	$\frac{k_{10,1}}{k_{2,1}}$
DFT	0.7390	-0.047	0.0088	-0.001 35	0.000 436	-0.002 87	0.50	-0.34
Exp	0.7416	-0.032	—	—	—	-0.001 70	0.71	-0.25

ADMR fitting procedures. Note that the  $c$ -axis dispersion is zero at  $\phi = 0^\circ$  and close to zero at  $\phi = 45^\circ$  as predicted by the ADMR fitting [8]. A detailed comparison of the fit parameters is shown in table 2. Overall, the fit parameters from the DFT calculation and dHvA/ADMR experiments are in good agreement. The sign and magnitude of all the terms agree well. The largest warping parameters  $k_{4,0}$  and  $k_{2,1}$  are experimentally found to be about 50% smaller than the DFT calculation; however, given the small size of these terms, the level of agreement is still remarkably good and gives additional confidence in the correctness of the experimental analysis. Finally, as shown in figure 11(b), the DFT calculation exhibits a decrease in the magnitude of  $k_{2,1}$  with decreasing doping, as we also found experimentally; however, the experimental doping dependence of  $k_{2,1}$  is much stronger than that predicted by DFT.

By performing rigid band shifts on the band-structure data for both the undoped Ti2201 calculation and the VCA calculation, we can estimate the variation of the Fermi surface extremal areas with band energy  $\varepsilon$ . Taking the derivative yields the band mass  $m_b = \frac{\hbar^2}{2\pi} \frac{\partial A}{\partial \varepsilon}$ . This band-structure determined mass, plotted as a function of doping in figure 11(a), includes lattice effects and electron–electron correlations at the mean field (LDA) level [46]. Given

<sup>7</sup> Note that the sign of  $k_{2,1}$  cannot be determined experimentally by either dHvA or ADMR and has thus been chosen to be negative to match that found by fitting band-structure calculations (see section 6).

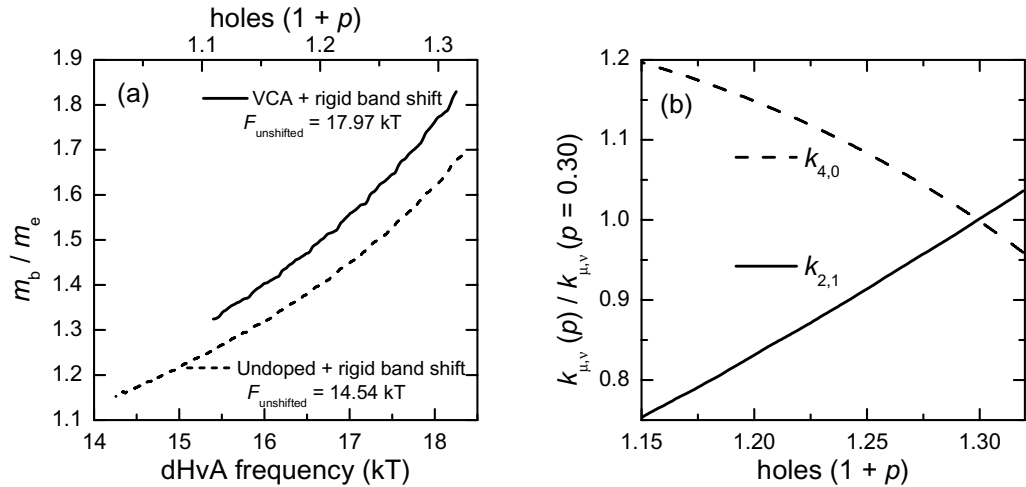


**Figure 11.** (a) Dependence of the DFT calculated band mass on the doping level which is adjusted by rigidly shifting the band energy. Calculations based on the undoped structure (dashed line) and the doped VCA calculation (solid line) are shown. (b) Doping dependence of the  $k_{4,0}$  (dashed line) and  $k_{2,1}$  (solid line) warping terms from rigid band shifts of the VCA calculation.

our uncertainties, the small predicted change in band mass would be unobservable between the two doping levels we have measured. However, the lack of any significant change in the electronic specific heat capacity [35] as  $T_c^{\text{max}}$  is approached is surprising. The difference between this band mass and the measured dHvA mass is a measure of the strength of the (dynamical) electron–electron correlations or electron–phonon interactions as discussed above. In the present case, the enhancement seems to be predominately driven by a correlation-induced band narrowing. It might be possible to account for this in the calculation by introducing an on-site potential within the LDA+U formulation [46]. At first sight it might be surprising that the detailed FS warping parameters agree so well with the band structure given the large discrepancy in the calculated band width. Note that although Luttinger’s theory means that the volume of the FS is conserved when many-body effects are included, the shape of the FS is not necessarily conserved. The fact that it is (approximately) points to the potential giving rise to the narrowing being highly isotropic.

## 7. Discussion

Prior to the breakthrough experiment in underdoped Y123 by Doiron-Leyraud *et al* [12], overdoped Tl2201 had always been considered as one of the best candidates for the observation of quantum oscillations in cuprates. Indeed, several of the present authors, our colleagues and other members of the community had tried, albeit unsuccessfully, to observe genuine quantum oscillations in Tl2201 for more than 15 years. In retrospect, it is not hard to understand now why it proved such a difficult task, in view of the fact that they have only been observed in a few per cent of the crystals studied.

So now that quantum oscillations are finally and unambiguously observed, what can we learn from them? First and foremost, the Fermi surface that we measure is the full one

predicted by the band structure in the absence of any reconstruction. This result implies that the pseudogap must close at some critical doping level inside the superconducting dome, i.e. that the normal state pseudogap and the superconducting gap are not coincident in the overdoped regime. One might counter, of course, that the magnetic field is acting to suppress any (small) pseudogap present in the heavily overdoped regime. However, quantitative comparisons between the properties calculated from the characteristics of the quasiparticles that we observe through quantum oscillations at high fields and those measured directly by transport [33], thermodynamic [35] and spectroscopic [37] measurements at low (and in some cases zero) field make this unlikely.

A more subtle question is whether the electronic ground state in overdoped Tl2201 is indeed a standard Fermi liquid. It is now known that while the  $T$ -dependence of the in-plane resistivity  $\rho_{ab}(T)$  in a heavily overdoped non-superconducting cuprate (LSCO) follows a strictly quadratic temperature dependence at low  $T$  [6], for superconducting Tl2201, an additional  $T$ -linear component persists down to very low temperatures [5, 34]. In LSCO, this non-Landau-Fermi-liquid power law is observed over a wide doping range [47], suggesting some form of anomalous or ‘extended’ quantum criticality. In the vicinity of a quantum critical point, there may be unusual energy dependences of the effective mass (or more precisely of the real and imaginary parts of the quasiparticle self-energy) that manifest themselves in an anomalous temperature dependence of the quantum oscillation amplitude [23]. In the present study however, we find that the conventional Fermi-liquid formula applies for the entire temperature region studied, down to  $T = 0.35$  K. Moreover, the data for Tl26K show that the Fermi liquid state is not restricted to the edge of the superconducting dome but extends a considerable distance inside the dome (at least up to  $0.3 T_c^{\max}$ ). It remains to be determined whether deviations from this generalized form appear at lower temperatures, as found for example in CeCoIn<sub>5</sub> [24], and further experiments down to millikelvin temperatures are envisaged for addressing this important point.

The insensitivity of the quasiparticle mass to doping is another interesting, related observation [35]. It is widely assumed that correlation effects become stronger as one approaches the Mott transition from the overdoped side. Transport studies on both overdoped Tl2201 [48] and LSCO [47], for example, have shown that while the magnitude of the isotropic  $T^2$  scattering rate remains approximately constant, the anisotropic  $T$ -linear component grows rapidly with decreasing doping. Due to causality [49], one might expect such a marked increase in the inelastic scattering rate to be reflected in a corresponding enhancement of the effective mass. In order to understand why this is not necessarily so, one needs to consider the often neglected momentum dependence of the effective interaction.

Because the electron self-energy,  $\Sigma(\mathbf{k}, \omega)$  (containing all of the many-body correlation effects), can in general depend on both frequency and momentum, the quasiparticle effective mass  $m^*$  can be written as

$$\frac{m^*}{m_b} = \frac{m_\omega}{m_b} \times \frac{m_k}{m_b}, \quad (30)$$

where the ‘ $\omega$ -mass’  $m_\omega$  is the inverse of the quasiparticle weight  $Z$ , i.e.

$$\frac{m_\omega}{m_b} = Z^{-1} = \left( 1 - \frac{\partial \text{Re} \Sigma(\omega)}{\partial \omega} \right), \quad (31)$$

and the ‘ $k$ -mass’  $m_k$  is given by the expression

$$\frac{m_k}{m_b} = \left( 1 + \frac{m_b}{\hbar^2 k_F} \frac{\partial \text{Re} \Sigma(k, \omega = 0)}{\partial k} \right)^{-1}. \quad (32)$$

Note here that  $m_b$  refers to the non-interacting band mass [50–52]. If we consider only the on-site Coulomb interaction as the origin of the electron correlation, the self-energy depends only on the quasiparticle energy  $\omega$ , i.e.  $\Sigma(\mathbf{k}, \omega) = \Sigma(\omega)$ . In this situation, one expects the effective mass to be strongly enhanced or to diverge as the (on-site) electron correlations become progressively stronger [53]. In the general case, however, where Coulomb interaction is non-local and the self-energy has a momentum dependence, the screening of the Coulomb potential is weak and the contribution of the momentum-dependent self-energy becomes significant, resulting in a possible decrease of the  $k$ -mass and a corresponding reduction in  $m^*$  [52, 54]. Thus, while correlation effects in cuprates become stronger with reduced doping, the fact that the anomalous interaction could be strongly  $k$ -dependent might act to suppress any corresponding enhancement in the effective mass.

Extensive theoretical and experimental work has suggested that hole-doping in cuprates is intrinsically inhomogeneous on a length scale of a few unit cells [55–58]. NMR experiments on Y123, however, suggest that (static) phase separation is *not* a generic property of underdoped or optimally doped cuprates [59]. This is supported by analyses of heat capacity data for Bi2212 over a wide range of hole doping  $p$  and of NMR data for Y124 and Ca-doped Y123 [60]. For overdoped cuprates, the applicability of the phase separation picture is still debated. Experimentally, the ratio of the superfluid density  $n_s$  to the carrier effective mass  $m_{\text{therm}}^*$  is found to decrease with increasing  $p$  [61, 62]. This so-called ‘boomerang’ effect has been attributed both to pair-breaking in a homogeneous electronic state [61] and to spontaneous phase separation into hole-rich (non-SC) and hole-poor (SC) regions [56, 62–64].

The observation of rapid quantum oscillations with a single frequency in overdoped Tl2201 appears to rule out the notion that coexisting hole-rich and hole-poor regions (of the order of the coherence length) are the origin of the decrease in  $n_s$  in this system. In the alternative, pair-breaking scenario, the rapid loss of superfluid density is attributed to a crossover from weak to strong pair breaking with overdoping [61]. According to our dHvA data, the intrinsic  $\ell_0$  is relatively insensitive to carrier concentration, and in LSCO at least, the residual in-plane resistivity  $\rho_{ab}(0)$  is roughly constant across the entire overdoped region of the phase diagram [47]. Thus, for the crossover from clean to dirty limit superconductivity to be realized, overdoping must be accompanied by a marked reduction in the strength of the pairing interaction [61, 65], as implied by the observed correlation between  $T_c$  and the magnitude of the (anisotropic)  $T$ -linear scattering rate in both overdoped LSCO [47] and Tl2201 [48].

In fully oxygenated LSCO, it is usually assumed that  $x$  equals  $p$ , the number of added holes per  $\text{CuO}_2$  unit. Tallon *et al* [18] have argued that  $T_c$  follows a universal dependence on  $p$  for *all* hole-doped cuprate families:  $T_c/T_c^{\text{max}} = 1 - 82.6(p - 0.16)^2$ . In many families however, the precise doping level is difficult to determine. The SC phase diagram of overdoped Tl2201 is compared with that of LSCO in figure 12. The dashed line is the ‘universal’ parabola [18], scaled to  $T_c^{\text{max}}$ , while the solid line is the corresponding  $T_c(p)$  curve for Tl2201, as determined by this study (black squares). (Here we have assumed that  $T_c^{\text{max}}$  remains at  $p = 0.16$ .) Extrapolation of the solid line in figure 12 to  $T_c = 0$  implies that superconductivity in Tl2201 will disappear at  $p = 0.31$ . In LSCO, the  $T$ -linear term in  $\rho_{ab}$  persists to  $x = 0.29$ , i.e. outside the LSCO SC dome [47], implying that pairing may still be active there. Indeed, comparison of the

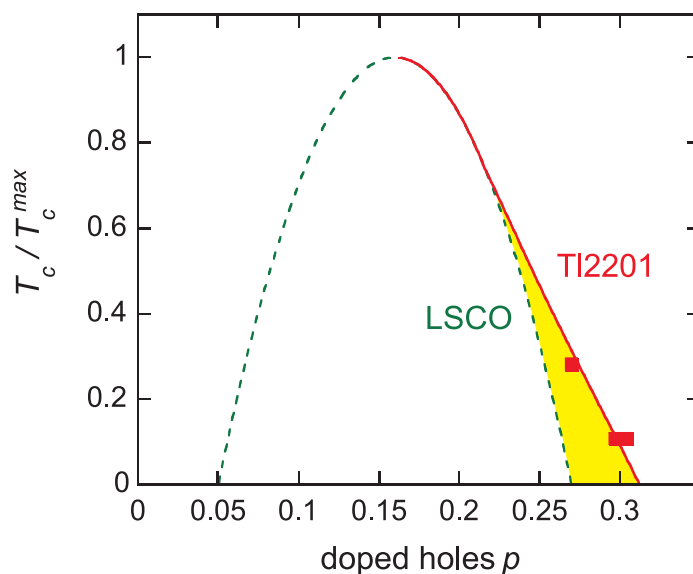


**Figure 12.** Schematic phase diagram of cuprates, based on the present data for TI2201 compared to those derived from measurements of LSCO.

impurity scattering rate with the superconducting gap energy  $\Delta_0$  suggests that the parabolic tail-off of  $T_c(p)$  in LSCO could be attributable to the same pair-breaking effects that lead to the reduction in  $n_s/m_{\text{therm}}^*$ . In LSCO ( $x = 0.29$ ),  $\rho_{ab}(0) \sim 18 \mu\Omega \text{ cm}$  [47]. Taking FS parameters for overdoping LSCO from ARPES [66], we obtain a transport (i.e. large-angle) scattering rate  $\hbar/\tau_0 \sim 10 \text{ meV}$  that is much larger than the BCS weak coupling value  $\Delta_0 = 2.14 k_B T_c \sim 2 \text{ meV}$ , for  $T_c \simeq 10 \text{ K}$ . In contrast, for TI2201 with  $T_c = 10 \text{ K}$ ,  $\rho_{ab}(0) \sim 6 \mu\Omega \text{ cm}$ , and correspondingly,  $\hbar/\tau_0 \sim 3 \text{ meV} \simeq \Delta_0$  [5, 64].

In other words, the extent of the superconducting dome in TI2201, with low levels of impurity scattering, is closely tied to the doping dependence of the underlying pairing interaction. However, the high levels of impurity scattering found in LSCO tend to prematurely kill off bulk superconductivity with increasing overdoping. Thus, the detailed shape of the  $T_c^{\max}$  versus  $p$  parabola, which had previously been thought to be universal to all cuprates, may in fact be a coincidence arising from the large intrinsic disorder found in LSCO.

## 8. Conclusion

In conclusion, detailed angle-dependent quantum oscillation experiments have uncovered a wealth of new information pertaining to the bulk electronic structure and superconductivity of the single-layer cuprate TI2201. All indicators suggest that the physical properties of overdoped TI2201 are determined by a single, spatially homogeneous electronic ground state and that there is no phase separation over a length scale of more than  $1000 \text{ \AA}$ . Combined with the NMR measurements on underdoped and optimally doped cuprates [59], it would appear that static nanoscale inhomogeneity and phase separation are not *intrinsic* features of cuprates *in any region of the phase diagram*. We therefore conclude that pair breaking (possibly enhanced by the effect of a pairing interaction that is highly anisotropic) is responsible for the loss of superfluid density in overdoped TI2201 and probably for the disappearance of superconductivity in LSCO below  $p_c = 0.31$ . The underlying reason for this appears to be the rapid fall in the

strength of the pairing interaction on the overdoped side [61, 65]. This, and the absence of any significant renormalization near the Fermi level, supports a purely magnetic or electronic pairing mechanism.

The observation of quantum oscillations in a regime where the transport properties show non-Fermi-liquid power laws is particularly intriguing. We have argued here that the lack of any doping dependence in the quasiparticle mass is possibly related to the strong momentum dependence of the electronic correlations [67]. A related question is how far into the superconducting dome do quantum oscillations survive as the carrier concentration  $p$  is decreased? Clearly this has a strong influence when choosing an appropriate starting point to describe the high- $T_c$  cuprates. Now that quantum oscillations are an active field in cuprate research, further measurements may well have an important role to play in developing our understanding of these key, fundamental issues.

## Acknowledgments

We thank L Balicas, A I Coldea, C Proust, D Vignolles, B Vignolle, M M J French, I Kokanović, A P Mackenzie, D A Bonn, W N Hardy, R Liang and B J Ramshaw for their contributions to this project. This work was supported by the EPSRC (UK), the Royal Society and a cooperative agreement between the State of Florida and NSF.

## References

- [1] Zaanen J *et al* 2006 *Nat. Phys.* **2** 138
- [2] For a review, see Hussey N E 2008 *J. Phys.: Condens. Matter* **20** 123201
- [3] Anderson P W 1997 *The Theory of Superconductivity in the High- $T_c$  Cuprates* (Princeton, NJ: Princeton University Press)
- [4] Loram J W, Mirza K A, Cooper J R, Liang W Y and Wade J M 1994 *J. Supercond.* **7** 243
- [5] Proust C, Boaknin E, Hill R W, Taillefer L and Mackenzie A P 2002 *Phys. Rev. Lett.* **89** 147003
- [6] Nakamae S, Behnia K, Mangkorntong N, Nohara M, Takagi H, Yates S J C and Hussey N E 2003 *Phys. Rev. B* **68** 100502
- [7] Yusof Z M, Wells B O, Valla T, Fedorov A V, Johnson P D, Li Q, Kendziora C, Jian S and Hinks D G 2002 *Phys. Rev. Lett.* **88** 167006
- [8] Hussey N E, Abdel-Jawad M, Carrington A, Mackenzie A P and Balicas L 2003 *Nature* **425** 814
- [9] Fowler C M, Freeman B L, Hults W L, King J C, Mueller F M and Smith J L 1992 *Phys. Rev. Lett.* **68** 534
- [10] Kido G, Katayama-Yoshida H and Takahashi T 1992 *J. Phys. Chem. Sol.* **53** 1555
- [11] Springford M, Harrison N, Meeson P J and Probst P-A 1992 *Phys. Rev. Lett.* **69** 2453
- [12] Doiron-Leyraud N, Proust C, LeBoeuf D, Levallois J, Bonnemaïson J-B, Liang R, Bonn D A, Hardy W N and Taillefer L 2007 *Nature* **447** 565
- [13] Yelland E A, Singleton J, Mielke C H, Harrison N, Balakirev F F, Dabrowski B and Cooper J R 2008 *Phys. Rev. Lett.* **100** 047003
- [14] Bangura A F *et al* 2008 *Phys. Rev. Lett.* **100** 047004
- [15] Vignolle B, Carrington A, Cooper R A, French M M J, Mackenzie A P, Jaudet C, Vignolles D, Proust C and Hussey N E 2008 *Nature* **455** 952
- [16] Bangura A F, Rourke P M C, Benseman T M, Matusiak M, Cooper J R, Hussey N E and Carrington A 2010 *Phys. Rev. B* **82** 140501
- [17] Helm T, Kartsovnik M V, Bartkowiak M, Bittner N, Lambacher M, Erb A, Wosnitza J and Gross R 2009 *Phys. Rev. Lett.* **103** 157002
- [18] Tallon J L, Bernhard C, Shaked H, Hitterman R L and Jorgensen J D 1995 *Phys. Rev. B* **51** 12911



- [19] Shoenberg D 1984 *Magnetic Oscillations in Metals* (Cambridge: Cambridge University Press)
- [20] Bergemann C, Brooks J S, Balicas L, Mackenzie A P, Julian S R, Mao Z Q and Maeno Y 2001 *Physica B* **294** 371
- [21] Bergemann C, Mackenzie A P, Julian S R, Forsythe D and Ohmichi E 2003 *Adv. Phys.* **52** 639
- [22] Hase I and Nishihara Y 1996 *J. Phys. Soc. Japan* **65** 3957
- [23] Wasserman A, Springford M and Han F 1991 *J. Phys.: Condens. Matter* **3** 5335
- [24] McCollam A, Julian S R, Rourke P M C, Aoki D and Flouquet J 2005 *Phys. Rev. Lett.* **94** 186401
- [25] Schlottmann P 2008 *Phys. Rev. B* **77** 195111
- [26] Springford M (ed) 1980 *Electrons at the Fermi Surface* (Cambridge: Cambridge University Press)
- [27] Carrington A *et al* 2003 *Phys. Rev. Lett.* **91** 037003
- [28] Analytis J G, Abdel-Jawad M, Balicas L, French M M J and Hussey N E 2007 *Phys. Rev. B* **76** 104523
- [29] Abdel-Jawad M, Kennett M P, Balicas L, Carrington A, Mackenzie A P, McKenzie R H and Hussey N E 2006 *Nature Phys.* **2** 821
- [30] French M M J, Analytis J G, Carrington A, Balicas L and Hussey N E 2009 *New J. Phys.* **11** 055057
- [31] French M M J 2009 *PhD Thesis* University of Bristol
- [32] Tyler A W 1997 *PhD Thesis* Cambridge University
- [33] Mackenzie A P, Julian S R, Sinclair D C and Lin C T 1996 *Phys. Rev. B* **53** 5848
- [34] Mackenzie A P, Julian S R, Diver A J, Lonzarich G G, Hussey N E, Maeno Y, Nishizaki S and Fujita T 1996 *Physica C* **263** 510
- [35] Wade J M, Loram J W, Mirza K A, Cooper J R and Tallon J L 1994 *J. Supercond.* **7** 261
- [36] Peets D C, Mottershead J D F, Wu B, Elfimov I S, Liang R, Hardy W N, Bonn D A, Raudsepp M, Ingle N J C and Damascelli A 2007 *New J. Phys.* **9** 28
- [37] Platé M *et al* 2005 *Phys. Rev. Lett.* **95** 077001
- [38] Hussey N E, Cooper J R, Wheatley J M, Fisher I R, Carrington A, Mackenzie A P, Lin C T and Milat O 1996 *Phys. Rev. Lett.* **76** 122
- [39] Manako T, Kubo Y and Shimakawa Y 1992 *Phys. Rev. B* **46** 11019
- [40] Grigoriev P D 2010 *Phys. Rev. B* **81** 205122
- [41] Blaha P, Schwarz K, Madsen G K H, Kvasnicka D and Luitz J 2001 *WIEN2k, An Augmented Plane Wave + Local Orbitals Program for Calculating Crystal Properties* (Karlheinz Schwarz, Techn. Universität Wien, Austria) ISBN 3-9501031-1-2
- [42] Perdew J P, Burke K and Ernzerhof M 1996 *Phys. Rev. Lett.* **77** 3865
- [43] Liu R S, Hughes S D, Angel R J, Hackwell T P, Mackenzie A P and Edwards P P 1992 *Physica C* **19** 203
- [44] Singh D J and Pickett W E 1992 *Physica C* **203** 193
- [45] Sahrakorpi S, Lin H, Markiewicz R S and Bansil A 2007 *Physica C* **460** 428
- [46] Petukhov A G, Mazin I I, Chioncel L and Lichtenstein A I 2003 *Phys. Rev. B* **67** 153106
- [47] Cooper R A *et al* 2009 *Science* **323** 603
- [48] Abdel-Jawad M, Analytis J G, Balicas L, Carrington A, Charmant J P H, French M M J and Hussey N E 2007 *Phys. Rev. Lett.* **99** 107002
- [49] Hussey N E 2005 *J. Phys. Soc. Japan* **74** 1107
- [50] Glyde H R and Hernadi S I 1983 *Phys. Rev. B* **28** 141
- [51] Greeff C W, Glyde H R and Clements B E 1992 *Phys. Rev. B* **45** 7951
- [52] Inoue I H, Hase I, Aiura Y, Fujimori A, Haruyama Y, Maruyama T and Nishihara Y 1995 *Phys. Rev. Lett.* **74** 2539
- [53] Brinkman W F and Rice T M 1970 *Phys. Rev. B* **2** 4302
- [54] Inoue I H, Goto O, Makino H, Hussey N E and Ishikawa M 1998 *Phys. Rev. B* **58** 4372
- [55] Emery V J and Kivelson S A 1993 *Physica C* **209** 597
- [56] Uemura Y J 2001 *Solid State Commun.* **120** 347
- [57] Pan S H *et al* 2001 *Nature* **413** 282
- [58] McElroy K, Lee J, Slezak J A, Lee D-H, Eisaki H, Uchida S and Davis J C 2005 *Science* **309** 1048



- [59] Bobroff J, Alloul H, Ouazi S, Mendels P, Mahajan A, Blanchard N, Collin G, Guillen V and Marucco J-F 2002 *Phys. Rev. Lett.* **89** 157002
- [60] Loram J W, Tallon J and Liang W Y 2004 *Phys. Rev. B* **69** 060502
- [61] Niedermayer Ch, Bernhard C, Binniger U, Glückler H, Tallon J L, Ansaldo E J and Budnick J I 1993 *Phys. Rev. Lett.* **71** 1764
- [62] Uemura Y J *et al* 1993 *Nature* **364** 605
- [63] Tanabe Y, Adachi T, Noji T and Koike Y 2005 *J. Phys. Soc. Japan* **74** 2893
- [64] Wang Y, Yan J, Shan L, Wen H-H, Tanabe Y, Adachi T and Koike Y 2007 *Phys. Rev. B* **76** 064512
- [65] Storey J G, Tallon J L and Williams G V M 2007 *Phys. Rev. B* **76** 174522
- [66] Yoshida T *et al* 2007 *J. Phys.: Condens Matter* **19** 125209
- [67] Gull E, Ferrero M, Parcollet O, Georges A and Millis A J 2010 *Phys. Rev. B* **82** 155101